Published in final edited form as:
Inorg Chem. 2010 April 19; 49(8): 3629–3645. doi:10.1021/ic9020993.

Heme-Copper/Dioxygen Complexes: Towards Understanding Ligand-Environmental Effects on Coordination Geometry, Electronic Structure and Reactivity

Zakaria Halime[†], **Matthew T. Kieber-Emmons**[‡], **Munzarin F. Qayyum**[‡], **Biplab Mondal**[†], **Simona C. Puiu**[†], **Eduardo E. Chufán**[†], **Amy A. N. Sarjeant**[†], **Keith O. Hodgson**[‡,#], **Britt Hedman**[#], **Edward I. Solomon**[‡,#], and **Kenneth D. Karlin**[†,§]

[†]Department of Chemistry, The Johns Hopkins University, Baltimore, MD 21218

[§]Department of Bioinspired Science, Ewha Womans University, Seoul 120-750, Korea

[‡]Department of Chemistry, Stanford University, Stanford, CA 94305

[#]Stanford Synchrotron Radiation Lightsource, SLAC, Stanford University, Stanford, CA 94309

Abstract

The nature of the ligand is an important aspect of controlling structure and reactivity in coordination chemistry. In connection with our study of heme/copper/oxygen reactivity relevant to cytochrome *c* oxidase O_2-reduction chemistry, we compare the molecular and electronic structure of two high-spin heme-peroxo-copper $[Fe^{III}\text{-}O_2^{2-}\text{-}Cu^{II}]^+$ complexes containing N_4-tetradentate (**1**) or N_3-tridentate (**2**) copper ligands. Combining previously reported and new resonance Raman and EXAFS data coupled to DFT calculations we report a geometric structure and more complete electronic description of the high-spin heme-peroxo-copper complexes **1** and **2,** which establish μ-(O_2^{2-}) side-on to the Fe^{III} and end-on to Cu^{II} (μ-η^2:η^1) binding for the complex **1** but side-on/side-on (μ-η^2:η^2) μ-peroxo coordination for the complex **2**. We also compare and summarize the differences and similarities of these two complexes in their reactivity toward CO, PPh_3, acid and phenols. The comparison of a new X-ray structure of μ-oxo complex **2a** with the previously reported **1a** X-ray structure, two thermal decomposition products respectively of **2** and **1**, reveals a considerable difference in the Fe-O-Cu angle between the two μ-oxo complexes (∠Fe-O-Cu = 178.2° in **1a**, ∠Fe-O-Cu = 149.5° in **2a**). The reaction of **2** with one equivalent of exogenous N-donor axial base leads to the formation of a distinctive low-temperature stable, low-spin heme-O_2-Cu complex (**2b**), but under the same conditions the addition of an axial base to **1** leads to the dissociation of the heme-peroxo-Cu assembly and the release of O_2. **2b** reacts with phenols performing hydrogen-atom ($e^- + H^+$) abstraction resulting in O-O bond cleavage and the formation of high-valent ferryl $[Fe^{IV}\text{=}O]$ complex (**2c**). The nature of **2c** was confirmed by comparison of its spectroscopic features and reactivity with those of an independently prepared ferryl complex. The phenoxyl radical generated by the hydrogen-atom abstraction was either 1) directly detected by EPR spectroscopy using phenols that produce stable radicals or 2) indirectly by detection of the coupling product of two phenoxyl radicals.

karlin@jhu.edu, edward.solomon@stanford.edu.

Supporting Information Available. UV-visible spectra of the reaction of (**2b**) with 1 equiv. of 2,4-di-*tert*butylphenol (Figure S1), UV-vis spectra of the reaction of $[(F_8)Fe^{III}\text{-}(O_2^{2-})\text{-}Cu^{II}(TMPA)]^+$ (**1**) with DMAP (Figure S2), EPR spectra of (**2b**) reaction with 1 equiv. of 2,4-di-*tert*-butylphenol (Figure S3), GC-MS trace of the oxidative coupling of 2,4-di-*tert*-butylphenol in presence of (**2b**) (Figure S4), ORTEP diagram (Figure S5) and crystal data and structure refinement for $[(F_8)Fe^{III}\text{-}(O^{2-})\text{-}Cu^{II}(AN)]^+$ (**2a**) X-ray structure (Table S1), XAS spectra and computational data.

Introduction

In the last few years, we have been engaged in heme/copper/O_2 reactivity studies using synthetic systems, with the goal being to provide fundamental information of possible relevance to biological heme-copper oxidases (HCO's) which include cytochrome *c* oxidase (C*c*O). HCO's are the terminal enzymes of the respiratory chain which catalyze the reduction of molecular oxygen to water, a process that requires four electrons and four protons,

$$\mathbf{O_2}+4-\ e^-\ (\text{from cyt}-\mathbf{c_{reduced}})+8\ \mathbf{H^+}\ (\text{from inside membrane})$$
$$->2\ \mathbf{H_2O}+4\ \mathbf{H^+}\ (\text{membrane translocated})+4\ \mathbf{cyt}-\mathbf{c_{oxidized}}$$

The reaction is coupled to the pumping of four additional protons across the mitochondrial or bacterial membrane which ultimately is utilized to drive ATP synthetase activity and thus generate ATP which is stored and used in subsequent metabolic functions.[1-6]

In the heme-copper active-site mediated O_2-reduction by HCO's, dioxygen reacts with a fully reduced $Fe^{II}\cdots Cu^{I}$ binuclear center (Scheme 1) initially forming a detectable transient, the $Fe^{III}–(O_2^{-})\cdots Cu^{I}$ complex **A**. **A** exhibits UV-vis and resonance Raman (rR) spectroscopic properties very similar to those known for oxy-hemoglobin or myoglobin. A DFT calculated structure of **A** supports the $Fe^{III}(O_2^{-})\cdots Cu^{I}$ formulation with the Cu ion positioned very close to the superoxo O-atom, Cu···O = 2.12 Å.[7] The next transformation seems optimized to prevent leakage of deleterious intermediates such as hydroxyl radical or hydrogen peroxide, wherein rapid overall four-electron reductive O–O cleavage is completed, giving $\mathbf{P_M}$, in which a closeby coupled Tyr (Scheme 1) or nearby Trp[8] residue efficiently provides a needed electron. A peroxo-bridged Fe^{III}-(O_2^{2-})-Cu^{II} transient has been discussed as possibly forming from **A** prior to $\mathbf{P_M}$ formation.[9-12] Also discussed and calculated is an electron-transfer from Cu_B^{I} in **A** which is accompanied by H^+ uptake to give a μ-hydroperoxo transient, Fe_{a3}^{III}-O-O(H)-Cu_B^{II}; the protonation event in this scenario would trigger electron transfer (from the heme a_3 and the Tyr244) yielding a cleaved O—O product ferryl moiety (state $\mathbf{P_M}$, Scheme 1).[10, 13-15]

Synthetic modeling presents a chemically interesting if not necessary approach to study metalloprotein active site structure (electronic and connectivity) and reactivity and its relationship with the inherent fundamental chemistry associated with the metal ion and its ligand environment.[16-18] Of particular interest is the **A** to $\mathbf{P_M}$ conversion, as O-O cleavage chemistry is of broad fundamental and practical importance in the utilization of molecular oxygen such as in biological "O_2-activation" occurring in heme, non-heme iron and copper oxidases or oxygenases. The use of O_2 (from air) in practical (chemical/industrial) organic oxidations, or energy production in fuel cell technologies also involves O-O cleavage. The reverse process, O-O bond formation, occcurs in photosynthesis and is of great contemporary interest and importance as related to worldwide energy concerns. This timely forum highlights the importance of understanding the elementary kinetic steps required to reductively cleave the O—O bond, and the many ways researchers are tackling such issues.

In this article we will highlight our own studies in the synthetic modeling of heme-copper oxidases, also providing new insights obtained on heme-Cu/O_2 adduct structure, bonding and reactivity. In our earlier studies, we have employed a systematic approach varying the design of heme/Cu complexes.[6] The approach entails synthetic modulation of copper ligand type, denticity, arrangement of donors, heme axial 'base' ligand and availability of protons or reducing equivalents. The overarching question is how such factors influence heme-copper/O_2 derived structures, along with the resulting complex Fe-O_2(H)-bonding and electronic structure (i.e., spin state, level of reduction of dioxygen, etc.). Such factors have been shown

or are expected to dictate the absence or presence of further reactivity, and the nature of such reactivity in the context of O-O cleavage chemistry. With similar emphases, in part, the research groups of Collman and coworkers[5,19] and Naruta and coworkers[20,21] have been very active and have made major contributions. Collman has also presented a longtime program in biomimetic electrode surface electrocatalysis of the four-electron O_2-reduction to water.[5,22,23] Despite the many achievements and advancements from all groups, there remains a considerable lack of detail concerning structure (i.e., of heme-Cu/O_2 derived adducts) and therefore we do not have firm correlations between structure/bonding and ensuing reactivity. The latter involves protonation and electron-transfer steps, for which a deeper understanding of the thermodynamics and timing or order is required.

In our initial attempts to mimic the O_2 reduction chemistry of C*c*O, we utilized TMPA-Cu^I complexes, where TMPA (tris(2-pyridylmethylamine)) is a tetradentate N_4 ligand. We observed that a low-temperature stable hemeFe^{III}-peroxo-Cu^{II} complex $[(F_8)Fe^{III}\text{-}(O_2^{2-})\text{-}Cu^{II}(TMPA)]^+$ (**1**, Chart 1) could be generated from the O_2 reaction with an equimolar mixture of $(F_8)Fe^{II}$ and $[Cu^I(TMPA)]^+$ (see discussion below), were F_8 = tetrakis(2,6-difluorophenyl) porphyrinate2−24 Structural investigation of the ensuing complex using resonance Raman (rR) and X-ray absorption (XANES and EXAFS) spectroscopies coupled to DFT calculations indicated that the peroxide unit is bound side-on to the high-spin iron(III) (overall hexa-coordinate with the iron out of the porphyrinate plane) and end-on to the copper(II) (overall penta-coordinate), thus an Fe^{III}-(μ-η^2:η^1-peroxo)-Cu^{II} coordination mode.[25,26] An intraperoxide stretching band was observed in the rR spectrum at 808 cm^{-1}.[24,25] The plausibility of such a coordination mode was affirmed by Naruta and co-workers, through crystallographic characterization of such a complex possessing a closely related ligand framework.[27] There, $\nu_{O\text{-}O}$ was determined to be 790 cm^{-1} (Figure 1).

We also established the same μ-η^2:η^1 coordination mode in three other peroxo complexes containing tetradenate copper ligands (Chart 1). In $[(^6L)Fe^{III}\text{-}(O_2^{2-})\text{-}Cu^{II}]^+$ (**3**), the tetradentate TMPA ligand is covalently appended to the periphery of a 2,6-difluorophenyl-substituted porphyrin and $\nu_{O\text{-}O}$ = 788 cm^{-1}.[28, 29] In $[(F_8)Fe^{III}\text{-}(O_2^{2-})\text{-}Cu^{II}(L^{N4OH})]^+$ (**5a**) and $[(F_8)Fe^{III}\text{-}(O_2^{2-})\text{-}Cu^{II}(L^{N4OMe})]^+$ (**5b**) the copper ligand is a modified version of TMPA were one pyridine is replaced by protected (**5b**) or non-protected (**5a**) imidazole-phenol moiety to mimic the cross-linked histidine-tyrosine in C*c*O active site. The O-O stretching frequencies in **5a** and **5b** are 813 cm^{-1} and 815 cm^{-1}, respectively.6,[30] Extensive previous (and ongoing) Cu^I/O_2 chemical investigations have shown that even subtle differences in ligand/denticity can dramatically change the nature of the copper–dioxygen adduct and its reactivity toward substrates.31,[32] Tetradentate ligands, such as TMPA, induce formation of end-on (μ-1,2) peroxo dicopper(II) structures (Chart 2), whereas tridentate ligands generate side-on (μ-η^2:η^2) peroxo dicopper(II) species.[33] The former possess relatively average $\nu_{O–O}$ values, typically above 800 cm^{-1} (Chart 2). However, the latter side-on complexes have reduced (< 760 cm^{-1}) $\nu_{O–O}$ values (Chart 2), ascribed to back bonding from copper to the peroxo antibonding σ* orbital, which considerably weakens the O–O bond.[34-36]

To compare and contrast the chemistry with that for heme-Cu system possessing tetradentate copper ligands, we expanded our study to heme-Cu systems containing tridentate copper ligands. Within that context, we reported the synthesis and the characterization of three high-spin heme-peroxo-Cu complexes with tridentate copper ligands (Chart 1): 1) $[(F_8)Fe^{III}\text{-}(O_2^{2-})\text{-}Cu^{II}(AN)]^+$ (**2**) (AN = bis(3-dimethylaminopropyl)amine),[37] 2) $[(F_8)Fe^{III}\text{-}(O_2^{2-})\text{-}Cu^{II}(L^{Me2N})]^+$ (**6**) (L^{Me2N} = *N,N*-bis[2-(2-pyridyl)ethyl]methylamine),[38] and 3) $[(^2L)Fe^{III}\text{-}(O_2^{2-})\text{-}Cu^{II}]^+$ (**4**) (^2L = tethered prophryn-*N,N*-bis[2-(2-pyridyl)ethyl]methylamine).[39,40] In concordance with expectations from copper-dioxygen homodimer chemistry (Chart 2), the three complexes present O-O stretching frequencies below 760 cm^{-1} thereby suggesting a side-on (μ-η^2:η^2) mode of coordination for the peroxo bridge. Thus, the heme-peroxo-copper

complexes depicted in Chart 1 were tentatively assigned as such.[40] In this paper, this point is addressed in detail, following new rR and EXAFS spectroscopic studies supported by DFT calculations.

Further, in this report we have selected $[(F_8)Fe^{III}\text{-}(O_2^{2-})\text{-}Cu^{II}(TMPA)]^+$ (**1**) and $[(F_8)Fe^{III}\text{-}(O_2^{2-})\text{-}Cu^{II}(AN)]^+$ (**2**) containing tetra- and tridentate copper ligands, respectively, to compare and contrast molecular structure, electronic-structure/bonding and resultant reactivity, combining some previously published information, along with new data. The overall goal is to contribute a better understanding of the relationship between the denticity of the copper ligand to the structure and reactivity of high-spin heme-peroxo-Cu complexes. We also describe the formation and initial characterization of a new related low-spin heme-peroxo-Cu complex and compare the high-spin and low-spin complexes in their reactivity toward phenols as hydrogen-atom ($H^+ + e^-$) donors.

Results and Discussion

Generation of High-Spin Heme-Peroxo-Cu Complexes

As mentioned, $[(F_8)Fe^{III}\text{-}(O_2^{2-})\text{-}Cu^{II}(TMPA)]^+$ (**1**) has been structurally characterized, through a variety of spectroscopic studies, computational chemistry and comparison to the Naruta complex. These possess a $\mu\text{-}\eta^2\text{:}\eta^1$-peroxo ligation. A major goal of the present work is to elucidate or confirm the $\mu\text{-}\eta^2\text{:}\eta^2$- side-on peroxo structure previously proposed for **4** (and thus **6**) employing $[(F_8)Fe^{III}\text{-}(O_2^{2-})\text{-}Cu^{II}(AN)]^+$ (**2**) for such studies; the latter possesses synthetically more accessible precursor components, and has been found to be more stable and amenable to spectroscopic interrogation.

As previously described, $[(F_8)Fe^{III}\text{-}(O_2^{2-})\text{-}Cu^{II}(TMPA)]^+$ (**1**) and $[(F_8)Fe^{III}\text{-}(O_2^{2-})\text{-}Cu^{II}(AN)]^+$ (**2**) can be cleanly generated by bubbling O_2 at low temperature through an equimolar solution of $(F_8)Fe^{II}$ and $[Cu^I(AN)](B(C_6F_5)_4)$ or $[Cu^I(TMPA)](B(C_6F_5)_4$,[6,37] Scheme 2. With tridentate chelating ligands for the copper ion, complexes **2**, **4** and **6** possess the same UV-Vis features in the Q-band region, but which are clearly distinguishable from those of **1**, **3** and **5** with their tetradentate copper ligands.[39] In the former case a 2nd prominent absorption occurs, e.g. at 538 nm for **2** (Scheme 2). Low-temperature ^1H NMR characterization of the μ-peroxo products **1** and **2** show a downfield-shifted pyrrole resonance at ~ 95 ppm which has been confirmed by ^2H NMR studies using the pyrrole-deuterated (d_8-F_8)Fe^{II} analogue) in the synthesis This finding exclude the possibility that the product observed is (i) the η^2-peroxo compound $[(F_8)Fe^{III}]_2\text{–}(O_2^{2-})$ (~ 17.5 ppm, −80° C), (ii) an iron–superoxide complex, that is, $(F_8)Fe^{III}\text{–}(O_2^-)$ (~ 8.9 ppm, −80° C), (iii) the ferryl species $(F_8)Fe^{IV}$=O (~ 3.5 ppm, −80° C) or (iv) $(F_8)Fe^{III}$–OH (~ 135 ppm, −80° C).[41] In fact, the 95 ppm pyrrole resonance is in the range expected for a high-spin Fe^{III} (d^5, S = 5/2) system which is strongly antiferromagnetically coupled to a Cu^{II} ion (d^9, S = 1/2), giving an overall S = 2 spin system (confirmed in **1** by solution magnetic moment measurement μ_{eff} = 5.1 μ_B at −40° C). Further, in the case of $[(F_8)Fe^{III}\text{-}(O_2^{2-})\text{-}Cu^{II}(TMPA)]^+$ (**1**) MALDI-TOF-MS reveal the presence of a dioxygen adduct with a stoichiometry of $(F_8)Fe$: $Cu^{II}(TMPA)$:O_2 = 1:1:1 ratio and solution mass spectral data give the correct O_2-drived moiety (for which m/z increases by four when using $^{18}O_2$).[26]

Coordination Geometry and Electronic Structural Comparisons of 1 and 2

Cu EXAFS—The k^3-weighted Cu K-edge EXAFS spectroscopic data and Fourier transforms (FT) of **2** are shown in Figure 2. The EXAFS fit parameters are given in Table 1. The first-shell EXAFS data were fit best with five Cu-O/N contributions at 2.00 Å.[42] The theoretical phase and amplitude parameters were calculated from a Cu-N path. Using a Cu-O path the best first-shell fit resulted in a coordination number of four. This difference in the first-shell

coordination is within the estimated 20-25% error. Split first-shell fits with a combination of one to four short Cu-O/N with one to four longer Cu-N/O were also performed. These fits gave higher error with the split in distance between the two paths less than the resolution of the data (0.14 Å). The paths corresponding to the FT peak in the R = 2–2.8 Å range was fit using single scattering (SS) and multiple scattering (MS) contributions from the AN alkyl backbone. The FT peak in the R = 2.8–3.8 Å range was fit with a Cu···Fe SS contribution at 3.62 Å with its corresponding MS Cu-O-Fe vector refined to 3.75 Å when both distances and σ^2 values were allowed to float independently for these paths. Linking the σ^2 values for these paths resulted in a fit with Cu···Fe distance of 3.63 Å and Cu-O-Fe MS distance of 3.76 Å with a σ^2 value of 627×10^{-5} Å^2. The Cu···Fe vector distance varied between fits to data of four different samples and with slightly different splines giving an average Cu···Fe distance of 3.63 ± 0.04 Å.

Fe EXAFS—The k^3-weighted Fe K-edge EXAFS spectroscopic data and FT of **2** are shown in Figure 3. The first backscattering shell was fit best using one Fe-O/N contribution at 1.94 Å and five Fe-N/O contributions at 2.09 Å. The second-shell FT peak in the R = 2–3 Å range was fit using the porphyrin pyrrole α carbon SS and MS contributions, along with the SS contribution from the meso carbons. The Fe···Cu contribution was fit at 3.64 Å with its corresponding MS Fe-O-Cu vector refined to 3.71 Å when the two σ^2 values were linked to each other. Floating the σ^2 values for these paths resulted in very similar fit parameters. The Fe···Cu vector was not required to get a good fit to the EXAFS data. This is because the SS and MS contributions from the porphyrin pyrrole β carbons interfere with the signal from the Fe···Cu interaction making the metal-metal vector hard to determine. The reliable distance of the Fe···Cu interaction was thus obtained from Cu EXAFS. The intensity in the R = 3.5–5 Å FT range was fit with SS and MS components from the pyrrole β and γ carbon atoms.

Comparison of EXAFS between 1 and 2—The Cu K-edge EXAFS and FT of frozen solutions of **1** and **2** are compared in Figure S6. Both species have a first-shell coordination of 5 Cu-N/O, which in the case of **1** can be split to obtain a short Cu-O/N of 1.87 Å. The two EXAFS patterns between k = 4–12 Å^{-1} are significantly different and account for the contrasting copper ligands and Cu···Fe vectors in the two species. The slight phase shift to lower k in **1** is consistent with a lenghthened Cu···Fe vector in **1** of 3.72 Å compared to 3.63 Å in **2**. The higher EXAFS intensity in **1** is reflected in the higher FT intensity in which a major difference is observed from R = 3–4 Å. The signal in this region originates from the Cu···Fe interaction, which in **1** is much more intense because the Cu-O-Fe MS is stronger than that in **2**. This difference arises from the more linear Cu-O-Fe angle of 150° in **1** compared to 134° in **2**. Both angles have been calculated from EXAFS parameters.[43] The deconvoluted sine waves from the SS and MS of Cu-Fe and Cu-O-Fe, respectively, are shown in Figure S8. A Cu-O-Fe angle of 150° is not enough to produce such an intense MS wave in **1**. Some of the intensity in the R = 3–4 Å region is a result of SS and MS contribution from the light atoms of TMPA. The remainder of the difference between R = 2.5–5 Å is due to the different SS and MS contributions from the pyridine versus the alkylamine side-chains.

The Fe K-edge EXAFS and FT of the solution data of **1** and **2** are compared in Figure S7. Both have a split first-shell with a short 1Fe-O/N at 1.92 Å and 1.94 Å, respectively, and 5Fe-N/O at 2.09 Å. The small changes in the first-shell FT are possibly from the different interference of the two sine waves in each system. The EXAFS beat patterns are very similar in both species. The higher intensity in **1** is again from the stronger Fe-O-Cu MS. This higher intensity translates into the FT peak at 3.5 Å in **1** that is missing in **2**. Both **1** and **2** have a very similar coordination environment around Fe as seen from the Fe EXAFS. The Fe K-edge and pre-edge (Figure S9) lend further support to the Fe being in a very similar coordination environment. The pre-edge peak intensity at ~7113.5 eV is a result of a 1s→3d transition that is dipole forbidden but quadrupole allowed. This peak gains intensity from 4p mixing into the 3d ground state. Distortion away from centrosymmetry increases 4p-3d mixing as the Fe is pulled out of the

heme plane. The similar pre-edge peak intensity in the two systems suggests that the peroxo binding to Fe is similar in both species, i.e. side-on, as a consequence of similar Fe coordination.

Resonance Raman Spectroscopy—The O—O stretching frequencies of both **1** and **2** have been previously reported as 810 and 756 cm^{-1} respectively,[24,37] indicating the peroxo character of the bound dioxygen moiety. However, the significant difference between these two energies was hypothesized as due to a distinct core geometry, namely a $\mu:\eta^2:\eta^2$ for **2** relative to the $\mu\text{-}\eta^2:\eta^1$ found in **1**. To evaluate this possibility and an alternative η^1 coordination mode at the Fe, rR spectroscopy was performed to assess the displacement of the iron out of the heme pocket. In particular, the energy of the oxidation and spin state sensitive marker band ν_4 was recorded. From the spectra in Figure 4, the ν_4 band of **2** is observed at 1362 cm^{-1} which compares well to that of **1** (1360 cm^{-1}). A bona fide end-on dioxygen bound heme, [(F_8)(THF)Fe(O_2)][24,26,38,44] with the iron in the porphryn plane was measured as a control, and exhibits a ν_4 of 1370 cm^{-1}.

Geometric Structures—Spin-unrestricted DFT calculations were performed using the BP86 functional on [(F_8)Fe-O_2-Cu(TMPA)]$^+$ (**1**) and [(F_8)Fe-O_2-Cu(AN)]$^+$ (**2**). The optimized structures are shown in Figure 5 and selected bond angles and distances are reported in Table 2. An optimized structure of a truncated model lacking phenyl rings of the heme of **1** was previously reported,[25,26] however, the full structure of **1** was reoptimized herein to facilitate structural comparisons between **1** and **2**. The metrical parameters of the $\mu:\eta^2:\eta^1$ Fe—O_2—Cu core in the present structure of **1** agrees well with the previously reported metrical parameters of the truncated model, and thus indicates that the heme phenyl substituents exhibit only a minor effect on the core. The core structure of **1** is likewise very analogous to that of the crystallographically characterized tethered complex of Naruta and co-workers,[27] {[(TMP)Fe]-O_2-[Cu(5MeTPA)]}$^+$. Both molecules display a degree of ruffling of the porphyrin macrocycles, a feature not observed in the previous calculations of **1**, presumably due to their lack of phenyl substituents. The ruffling causes the four coordinating nitrogen atoms to deviate slightly from planarity. Thus, the displacement of the Fe out of the heme pseudo-plane (0.56 Å in the case of **2**) is reported as an average displacement.

In contrast to the $\mu\text{-}\eta^2:\eta^1$ structure of **1**, the geometry optimized core structure of **2** displays the peroxo moiety spanning the metals in a $\mu:\eta^2:\eta^2$ configuration, where the peroxo ligand has gone from η^1 to η^2 on Cu in going from **1** to **2**. This is the first example of such coordination in heme-peroxo-Cu chemistry. The most notable metrical parameters predicted by DFT of **2** and listed in Table 2 are: 1) an O—O bond length of 1.463 Å, 2) an intermetallic Fe···Cu distance of 3.727 Å, 3) slightly inequivalent Cu—O bond lengths of 2.094 and 2.001 Å (compared to the η^1 structure of **1**, where a Cu-O bond length of 1.945 Å is calculated), 4) slightly inequivalent Fe—O bond lengths of 2.060 and 1.902 Å, 5) a slight butterfly of the peroxo core characterized by an Fe—O—O—Cu dihedral angle of 166.1°, and 6) displacement of the Fe out of the pseudo-plane of the porphyrn by 0.53 Å. In general, the structural parameters predicted by theory are in good agreement with those measured by Fe and Cu K-edge EXAFS. In particular, DFT predicts an intermetallic distance (3.727 Å) in good agreement with the Fe···Cu vector observed from Cu and Fe EXAFS (3.63 Å). Furthermore, the predicted O—O bond length (1.463 Å) is well within the classical peroxo manifold. Analytical frequency calculations were performed on **1** and **2**, yielding $\nu_{O—O}$ energies of 889 and 821 cm^{-1} respectively, which parallel the observed ordering and difference of 810 and 756 cm^{-1} derived experimentally in **1** compared to **2**. Thus, the optimized core is well described by the calculations. Alternative coordination modes were assessed to ensure that a global minimum had been obtained. Specifically, a $\mu:\eta^2:\eta^1$ core geometry was found to be a local minimum on the HS potential energy surface. However, this coordination mode lies higher in energy then the $\mu:\eta^2:\eta^2$ (by ~ 65 kcal/mol), and deviates from the experimentally observed Fe···Cu distance by 0.5 Å (the predicted distance for this coordination mode is ~ 4.2 Å).

Electronic Structure—In agreement with the experimentally determined spin of the complexes, both molecules are well described by broken-symmetry wavefunctions, yielding $S_T = 2$ ground state electronic structures, in which the Fe^{III} and Cu^{II} are anti-ferromagnetically coupled. In both molecules, one α-hole is localized on the Cu whereas five β-holes are localized on the Fe (Figures 4 and 5),[45] The magnitude of the coupling in **1** and **2** between the $S_T = 2$ and $S_T = 3$ states, $|-6J|$, calculated using Equation 1, is 4552 and 4627 cm^{-1} respectively (using the Hamiltonian $-2JS_1 \bullet S_2$), and is in general agreement with the experimentally observed strong antiferromagnetic coupling. However, the nature of the ligands on copper, specifically the denticity, engenders distinct character to the singly occupied, and thus net bonding, orbital on the Cu. In the case of **1**, given the propensity of TMPA for 5-coordinate trigonal bypyramidal molecular geometry with O_2^{2-} bound in a end-on fashion, the singly occupied orbital is of $3d_z2$ character. In contrast, with the less conformationally demanding AN ligand which allows for square pyramidal geometry and bi-dentate O_2^{2-}, the singly occupied Cu d orbital of **2** is of $3d_{x^2-y^2}$ character. As depicted graphically in Figure 6, the superexchange pathways in **1** and **2** are via the sigma bonding framework. Specifically, the coupling involves the $3d_{xz}$ orbital of the Fe (z ∞ to the heme plane and x ∥ to the O—O vector) with the singly occupied orbital of the Cu, $3d_z2$ of $3d_{x^2-y^2}$ respectively.

In both molecules, the Fe-O_2^{2-} bonding is characterized by two interactions (Figures S5 and S6). The in-plane σ interaction is between the Fe $3d_{xz}$ and the O_2^{2-} π^*_σ orbitals and the out-of-plane δ interaction is between the Fe d_{xy} and the O_2^{2-} π^*_v orbitals. The orbital basis for the interactions are similar in **1** and **2**, but do reflect the differences in peroxo-copper bonding (Tables 3 and 4). In the case of **1**, the spin down σ bonding contributions are 12.0 % and 39.4 % for O_2^{2-} and Fe (Figure 4, Table 3, orbital β310) and the δ bonding contributions are 15.9 % and 76.7 % for O_2^{2-} and Fe (Figure 4, Table 3, orbital β303). In **2**, the spin down σ bonding contributions are 18.5 % and 61.9 % for O_2^{2-} and Fe (Figure 5, Table 4, orbital β284) and the δ bonding contributions are 13.4 and 80.5 % for O_2^{2-} and Fe (Figure 5, Table 4, orbital β279). Given that the Fe-porphyrin fragments in **1** and **2** are identical, any differences in bonding must be a result of modulation of the Cu fragment-peroxo bonding. As can be observed from the unoccupied spin-up Cu-O_2^{2-} anti-bonding molecular orbital of **1**, the Cu $3d_z2$ (38.7%) interacts strongly with the in-plane O_2 π^*_σ (31.9%), which does contain some contribution from the Fe (10.9%) and ligands (Figure 4, Table 3, orbital α307). The unfilled spin-up Cu-O_2^{2-} anti-bonding orbital of **2** indicates σ-overlap of the $3d_{x^2-y^2}$ (41.4%) with the in-plane O_2 π^*_σ (29.6%), with some Fe (9.7%) and ligand contributions (Figure 5, Table 4, orbital α283). In both molecules, the out-of-plane O_2 π^*_v is largely non-bonding with the otherwise filled Cu d manifold.

Comparison to the bonding observed in μ-η^2:η^2 and μ-η^1:η^1 Cu_2O_2 homo-dimers is instructive.[46] In the side-on peroxo complex, [{Cu(Tp)}$_2$-(O_2)], which displays a relatively low $\nu_{O—O}$ of ~760 cm^{-1}, the unoccupied Cu d – O_2 π^*_σ orbital was calculated to be composed of 68 % Cu and 22 % O_2. In contrast, in the end-on complex [{Cu(TMPA)}$_2$-(O_2)]$^{2+}$, which displays a $\nu_{O—O}$ of 830 cm^{-1} , the unoccupied Cu d – O_2 π^*_σ orbital consists of 43 % Cu and 9 % O_2. Thus, the low intraperoxide stretch observed in the side-on case was not a result of differences in the σ bonding framework (i.e. in the side-on complex [{Cu(Tp)}$_2$-(O_2)], the peroxo is a better π^*_σ donor which removes e^- density from an anti-bonding orbital, thus, the $\nu_{O—O}$ should be greater), but rather backbonding into the O_2^{2-} σ* (O_2^{2-}σ* mixing into occupied, predominantly Cu d orbitals).[47] On this basis, the ~2.3 % calculated difference in Cu-O_2 covalency in the σ framework of **1** and **2** does not sufficiently explain the ~50 cm^{-1} downward shift in the intraperoxide stretching energy observed experimentally between **1** and **2** (**2** having more π^*_σ character) and reproduced by DFT calculations. The more covalent (as defined by the mixing of the filled peroxo π^*_σ orbital into the unfilled Cu d orbital) σ interaction in fact would argue for a *higher* $\nu_{O—O}$ in **2**, inconsistent with experiment. Differences in mechanical coupling as a rationale to account for the lower intraperoxide stretch were also considered, but

determined to be negligible by systematically increasing the mass of the Cu bound ligand atoms. Surveying the occupied valence orbitals of **1** and **2** for O_2^{2-} σ* character indicates ~ 4x greater σ* character in the occupied valence orbitals of **2** compared to those of **1**. The σ* in **2** acts as a π-acceptor, which weakens the O—O bond, leading to a low $\nu_{O—O}$ stretching energy. Due to the fact that the σ* orbital is strongly antibonding, a few percent increase of the mixing of the σ* character into an occupied metal based orbital is enough to greatly impact the observed $\nu_{O—O}$. Thus, as for in the Cu_2O_2 dimers, the low observed $\nu_{O—O}$ in **2** is a result of σ* backbonding in the μ-η^2:η^2 core structure.

$$^4E=\frac{6^{BS}E-{}^6E\left(\left\langle S^2\right\rangle_{BS}-6\right)}{12-\left\langle S^2\right\rangle_{BS}} \qquad \text{Eq. 1}$$

Thermal Decomposition of 1 and 2—The thermal decomposition of high-spin heme-peroxo-Cu complexes **1** and **2** yields the corresponding μ-oxo compound $[(F_8)Fe^{III}\text{-}(O^{2-})\text{-}Cu^{II}(TMPA)]^+$ (**1a**) and $[(F_8)Fe^{III}\text{-}(O^{2-})\text{-}Cu^{II}(AN)]^+$ (**2a**) with distinct UV-vis bathochromic shifts in their Soret and Q bands (**1**: λ_{max} = 412, 526 nm;[48] **1a**: λ_{max} = 433, 553 nm[49,50] and **2**: λ_{max} = 418, 538, 561 nm; **2a**: λ_{max} = 440, 557 nm). The μ-oxo complexes also have distinct ^{1}H-NMR features at –80° C with a pyrrole resonance signal at ~105 ppm. Separate measurements[29] indicate that ~0.5 equiv. of dioxygen is released during the μ-peroxo to μ-oxo conversion, indicating this process involves a disproportionation reaction, 2 $[Fe^{III}\text{-}(O_2^{2-})\text{-}Cu^{II}]^+ \rightarrow 2\ [Fe^{III}\text{-}(O^{2-})\text{-}Cu^{II}]^+ + O_2$. Insights into the mechanism(s) for such reactions have not been sought or obtained, but similar kinds of processes are known and studied for related non-heme diiron species.[51,52]

X-ray Structure of μ-oxo complex $[(F_8)Fe^{III}\text{-}(O^{2-})\text{-}Cu^{II}(AN)]^+$ (2a)—The comparison between a new X-ray structure of $[(F_8)Fe^{III}\text{-}(O^{2-})\text{-}Cu^{II}(AN)]^+$ (**2a**), presented here (also see Supporting Information), and the previously described X-ray structure of $[(F_8)Fe^{III})\text{-}(O^{2-})\text{-}Cu^{II}(TMPA)]^+$ (**1a**)[49] (Figure 7), reveals that in both cases the metal-oxygen bond distances are all similar and characteristically short.[53,54] The Fe-O bond length in **1a** [1.740 Å] and **2a** [1.747 Å] are similar to those of μ-oxo-diiron(III)-(porphyrinates),[55] and the short Cu-O bond distances [1.856 Å in **1a** and 1.815 Å in **2a**] are not far off from values observed for bis-μ-oxodicopper(III) complexes (Cu-O = 1.8 Å).33,56 To further compare, a high-spin (heme) Fe^{III}-hydroxide Fe-O bond lengths is 1.86 Å,[57] while for example Cu^{II}-hydroxide Cu-O(H) bond lengths in complexes with the Cu^{II}-O(H)-Fe^{III} (1.89-1.95 Å)[50,58] or $Cu^{II}_2(OH^-)_2$ / $Cu^{II}(OH^-)$ core (1.9 – 2.0 Å) are greater.[59-67]

Most interestingly, there is a large difference in the $\angle Fe-O-Cu$ bond angle between the two structures. Complex **1a**, as most other (porphyrinate)Fe^{III}-O-Cu^{II} complexes with tetradentate copper ligands,[4,6] have near-linear core structures, but the Fe-O-Cu bridge in **2a** is severely bent to an angle of 149.5° as observed in the other complex $[(F_8)Fe^{III}\text{-}O\text{-}Cu^{II}(L^{Me2N})]^+$ (**6**) with tridentate copper ligand.[38] We note that a somewhat related μ-hydroxo complex, [(OEP) Fe-(OH)-Cu(Me_5dien)($OClO_3$)]($C1O_4$) (OEP = octaethylporphyrinate^{2-}); Me5dien = tris(2-(N,N-dimethylamino)-ethyl)amine), possesses a bent Fe^{III}-(OH^-)-Cu^{II} core ($\angle Fe-(OH)-Cu=157.0°$),[58] as would be expected for a protonated oxo group changing its hybridzation from ***sp*** (μ-oxo) to ***sp²*** (μ-hydroxo). For the μ-oxo complexes $[(F_8)Fe\text{-}(O^{2-})\text{-}Cu(TMPA)]^+$ (**1a**) and $[(F_8)Fe\text{-}(O^{2-})\text{-}Cu(AN)]^+$ (**2a**), the differences in observed structures once again illustrate how the nature of the copper chelate (tri- *versus* tetradentate) influences the structure of heme-copper/dioxygen adducts. Such structural (Chart 2) and reactivity effects are already well known in copper-dioxygen chemistry.[31,32,68]

Reactivity of high-spin heme–peroxo–copper complexes 1 and 2

We have previously[37] described the reactivity of [(F_8)Fe-(O_2^{2-})Cu(TMPA)]$^+$ (**1**) and [(F_8)Fe-(O_2^{2-})-Cu(AN)]$^+$ (**2**), along with peroxo complexes **3** and **4** (Chart 1), toward different reagents, HCl, $Co(Cp)_2$, CO, PPh_3 and ^{t}Bu-substituted phenols. As an important goal of the current report is to contrast reactivity when the spin-state of the heme-iron is changed (vide infra), we summarize here major aspects of the reactivity observed for the HS complexes **1** and **2** (Scheme 3).

Hydrochloric acid was added to **1** and **2**, in order to study the possibility of forming and studying protonated dioxygen species (e.g. hydroperoxo complexes).[9,10,12] Protonation and formation of such species are likely important in triggering HCO enzymatic O-O reductive cleavage events. When peroxo complexes **1** and **2** were exposed to one or two equivalents of HCl, neither low-temperature UV-vis nor ^{1}H NMR spectroscopic investigations showed any evidence for a hydroperoxo intermediate, i.e., formation of a new absorption feature was not found in the reaction. Further, electron paramagnetic resonance (EPR) spectroscopic and ESI-MS analyses of the reactions products revealed the formation of F_8Fe^{III}-Cl and Cu^{II}-Cl. H_2O_2 was released providing complementary evidence that O_2 adducts **1** and **2** have a peroxidic nature.[37]

Peroxo complexes **1** and **2** possess dioxygen in its two-electron reduced state. Thus, to complete the reductive cleavage of dioxygen to the level of water, two more electrons are needed. The strong outer-sphere reductant cobaltocene ($CoCp_2$) was, thus, used to provide these reducing equivalents.[29,37,48] Reaction of two equivalents of $CoCp_2$ does effect O-O cleavage and the formation of the corresponding previously structurally characterized μ-oxo-bridged compounds [(F_8)Fe^{III}-(O^{2-})-Cu^{II}(TMPA)]$^+$ (**1a**) and [(F_8)Fe^{III}-(O^{2-})-Cu^{II}(AN)]$^+$ (**2a**).[37] This result differs from an earlier work of Collman and coworkers where they showed that the addition of $CoCp_2$ to heme–dioxygen-copper complexes containing appended imidazole axial base for iron lead to fully reduced Fe^{II}/Cu^I and the reduction of O_2 to H_2O_2.[69-72]

1 and **2** were also exposed to carbon monoxide and PPh_3,[37] reagents known to either displace the peroxide or to be subject to oxidation giving CO_2 (in the case of CO (in C*c*O))[73] or O=PPh_3 in the case of triphenylphosphine. Compound **2** reacted with excess $CO_{(g)}$ to form the CO-adduct (THF)(F_8)Fe^{II}-CO and copper monoxide adduct [Cu^I(AN)(CO)]$^+$ while also releasing dioxygen. Surprisingly, **1** does not react with CO. **2** reacts with PPh_3 to displace the peroxo ligand from copper, but not from iron, thus involving a formally partial reduction reaction. The products are the iron–superoxo species (solvent)(F_8)Fe^{III}–($O_2^{\bullet-}$) and the reduced Cu^I–phosphine adduct [Cu^I(AN)(PPh_3)]$^+$. Interrogation of the product solutions using ^{31}P-NMR spectroscopy showed only the presence of PPh_3 (and no O=PPh_3). Unexpectedly, complex **1** displays no reaction toward PPh_3 under these conditions. In summary, there are clear differences in Fe^{III}–(O_2^{2-})–Cu^{II} reactions with CO or PPh_3 that reflect variations in the detailed nature of the peroxo structure and reactivity induced by the nature of the copper ligand (tri- *vs* tetradentate).

The examination of the addition of phenols to heme–Cu/O_2 adducts was inspired by reactivity observed for the "mixed-valent" C*c*O enzyme form, wherein an active-site tyrosine, found crystallographically to be covalently tethered to a copper bound histidine, is thought to act as a net hydrogen atom donor (see the Introduction and further discussion below).[4] When either 2,4-*t*Bu_2-phenol or 2,4,6-*t*Bu_3-phenol, i.e. good hydrogen atom ($H^+ + e^-$) donors, was added to low-temperature solutions of **1** or **2**, no reaction occured (Scheme 3). This is an important finding, especially when contrasted with the chemistry of a low-spin analog (vide infra).

Collman and co-workers[74] recently reported that a phenol as hydrogen-atom source can be added to a heme–superoxo–copper complex, (i.e. a low-spin $Fe^{III}(O_2^{\bullet-})\cdots Cu^I$ moiety) resulting in reductive O—O cleavage and formation of a phenoxyl radical (A, Chart 3). This heme–Cu

complex possesses an internal (i.e., appended) imidazole axial base for iron. A closely related complex possessing an internal phenol group (i.e., with one of the R-groups, Chart 3 (A), is a phenol) can electrocatalytically reduce dioxygen to water.[22] In that system, electronic structural and spin-state issues have not been addressed beyond the superoxo complex and possible intermediates after O-O cleavage. In systems we have studied, $(F_8)Fe^{III}(O_2^{-})\cdots Cu^{I}$ species are transient (but detectable) intermediates (Figure 8)[39] in the reduction of O_2 from the $Fe^{II}\cdots Cu^{I}$ to Fe^{III}-(O_2^{2-})-Cu^{II}((ligand) complex stage, the latter being stable at –80° C and amenable to study, i.e., those complexes in Chart 1.

It is notable that for non-heme iron Fe^{III}–OOR complexes, low-spin rather than high-spin species are amenable to reductive O−O cleavage chemistry as a consequence of weakened peroxide O−O bonds and strengthened Fe–O bonds.[75,76] From all the information available, as discussed thus far in this report, it was clear one should investigate, compare and contrast the chemistry of high-spin Fe^{III}–(O_2^{2-})–Cu^{II} complexes with low-spin analogues, if we could generate the latter. This was accomplished, as described below.

Generation of a low-spin heme-peroxo-copper Complex

The low-spin heme−O_2−copper complex which we formulate as $[DCHIm(F_8)Fe^{III}$-(O_2^{2-})-$Cu^{II}(AN)]^+$ (**2b**) was generated by the addition of one equivalent of 1,5-dicyclohexylimidazole (DCHIm) to a solution of high-spin $[(F_8)Fe^{III}$-(O_2^{2-})-$Cu^{II}(AN)]^+$ (**2**) in THF at -80° C (Scheme 4). Collman's research group reported the first example of a well-characterized discrete dioxygen adduct in a heme/Cu assembly using a sophisticated superstructured “capped” porphyrin with appended triazacyclononane as ligand for copper (B, Chart 3).[69,71] When a solution of $[(\alpha_3TACN\alpha Acr)Fe^{II}Cu^{I}]^+$ is mixed with large excess (500 equiv.) of DCHIm and subsequently exposed to dioxygen, rapid and irreversible formation of a low-spin adduct $[(DCHIm)(\alpha_3TACN\alpha Acr)Fe^{III}$–$(O_2^{2-})$-$Cu^{II}]^+$ occurs.

With our system, the UV-vis monitoring show that only one equivalent of DCHIm is required for the complete transformation of high-spin species **2** (418, 538, 561 nm) to low-spin species $[(DCHIm(F_8)Fe^{III}$-(O_2^{2-})-$Cu^{II}(AN)]^+$ (**2b**) (421, 537 nm) (Figure 9). A ^{2}H-NMR study of **2b** formation was performed using pyrrole-deuterated version of F_8 (Figure 10). After the generation of the high-spin peroxo (**2**) (pyrrole resonance at ~ 95 ppm), the addition of 1 equiv. of DCHIm is accompanied by the shift of the pyrrole signal to the diamagnetic region ($\delta_{pyrrole}$ ~ 8.3 ppm). This behavior suggests that in **2b**, the presence of antiferromagnetic coupling between the low-spin (S = 1/2) six-coordinate Fe(III) and the d^9 Cu(II) (also S = ½) centers occurs through the peroxo bridge. The latter's peroxidic nature is not yet unequivocally determined.[77] However, evidence that that $[DCHIm(F_8)Fe^{III}$-(O_2^{2-})-$Cu^{II}(AN)]^+$ (**2b**) possesses a peroxidic intact O-O bond is suggested by its reactivity with hydrochloric acid to release hydrogen peroxide in good yield (see Experimental Section). Alternative formulations of the new species **2b** as either 1) a mixture of $(F_8)Fe^{III}$-(O_2^{2-})-$Fe^{III}(F_8)$ ($\delta_{pyrrole}$ 15-19 ppm}, [26] and $[(AN)Cu^{II}$-(O_2^{2-})-$Cu^{II}(AN)]^+$ (formed by disproportionation of **2b**) or 2) a O—O cleaved[78] product give ferryl complex $[(DCHIm)(F_8)Fe^{IV}=O]$ (**2c**) ($\delta_{pyrrole}$ 4-5 ppm), can be ruled out based on its $\delta_{pyrrole}$ ~ 8.3 ppm assignment and UV-vis spectroscopic peak positions. [41] The formation of an analogous complex to **2b** was also observed using 4-(dimethylamino) pyridine (DMAP) instead of DCHIm as the exogenous axial ligand.

By contrast, the addition of an axial base such as DCHIm or DMAP to a solution of $[(F_8)$ Fe^{III}-(O_2^{2-})-$Cu^{II}(TMPA)]^+$ (**1**) effects the release of O_2 and the formation of a mixture of $[Cu^{I}(TMPA)]^+$ and six-coordinate low-spin compound $(F_8)Fe^{II}$–$(Base)_2$ (Scheme 4). The reaction was followed by UV-vis spectroscopy as shown in the Supporting Information (Figure S2): the peroxo compound **1** exhibits Q band at 558 nm with a shoulder at 535 nm (CH_3CN, – 40° C) and upon addition of 1 to 5 equiv. of DMAP a new spectrum with λ_{max} = 527 nm is formed assigned to $(F_8)Fe^{II}(DMAP)_2$. To support this assignment a control experiment was

conducted in which the addition of DMAP to a solution of the mixture of $(F_8)Fe^{II}$/$[Cu^{I}(TMPA)]^{+}$ yielded the same spectrum because of the formation of $(F_8)Fe^{II}(DMAP)_2$. The evolution of 0.9 equiv O_2 was determined by exposing evolved gases to an alkaline pyrogallol test solution;[79] within experimental error, this finding is consistent with the quantitative oxidation of the peroxide moiety to molecular oxygen.

Reactivity of low-spin peroxo $[DCHIm(F_8)Fe^{III}\text{-}(O_2^{2-})\text{-}Cu^{II}(AN)]^{+}$ complex (2b) toward phenols

To study the reactivity of the low-spin peroxo $[DCHIm(F_8)Fe^{III}\text{-}(O_2^{2-})\text{-}Cu^{II}(AN)]^{+}$ (**2b**) complex toward phenols, 2,4-*t*Bu_2-phenol was employed first as substrate. The rationale for selection of this phenol was if hydrogen atom abstraction ($H^{+} + e^{-}$) occured, the phenol would couple to form 3,3',5,5'tetra-tert-butyl-2,2'-dihydroxylbiphenyl which can be detected and quantified as stable product.[80-84] We have shown above (Scheme 3) that the high-spin peroxo complex **2** doesn't react with phenols. The addition of 1 equiv. of 2,4-*t*Bu_2-phenol to a solution of low-spin peroxo complex **2b** in THF at -80° C leads to the formation of the coupled phenol product (3,3',5,5'tetra-*tert*-butyl-2,2'-dihydroxylbiphenyl) (Scheme 5). GC-MS analyses of the reaction mixture at room temperature revealed that the yield of the reaction is greater than 65%. Further spectroscopic investigations show that the oxidative coupling of the phenol is accompanied by the reductive cleavage of the peroxo bridge and the formation of Cu^{II}-hydroxide complex ($[Cu^{II}(AN)(OH)]^{+}$) and ferryl heme $[(DCHIm)(F_8)Fe^{IV}{=}O]$ (**2c**) (Scheme 5). The evidence for the presence of $[Cu^{II}(AN)(OH)]^{+}$ comes from observation of a characteristic Cu^{II}-OH EPR signal of the frozen reaction mixture ($A_{\|} = 127 \times 10^{-4}$ cm^{-1}, $A_{\infty} = 35 \times 10^{-4}$ cm^{-1}, $g_{\|} = 2.24$ and $g_{\infty} = 2.06$) (Figure S3) and from ESI-MS spectrometry at room temperature (calculated m/*z* = 267.1 for $C_{10}H_{26}CuN_3O$; found, m/*z* = 267.5). The EPR spectrum of the reaction mixture after warming up to room temperature presents the same signal for Cu^{II}-OH in addition to a characteristic signal for the well known stable compound $(F_8)Fe^{III}$-OH (g = 5.8), which derives from thermal decay of $[(DCHIm)(F_8)Fe^{IV}{=}O]$ (**2c**).[41] The UV-vis monitoring of the O-O cleavage reaction shows a shift of the **2b** Q band at 535 nm to a new band at 540 nm (Supporting Information, Figure S1). This band was also observed for an authentic $[DCHIm(F_8)Fe^{IV}{=}O]$ generated by the reaction of $[(F_8)Fe^{III}]_2\text{-}(O_2^{2-})$ with DCHIm in noncoordinating solvent.[41,85] The ferryl nature of the product solution and presence of **2c** was also established by its reactivity toward different substrates: (a) the low-temperature addition of one equivalent of $[Cu^{I}(AN)]^{+}$ leads to the formation of $[(F_8)Fe^{III}\text{-}(O^{2-})\text{-}Cu^{II}(AN)]^{+}$ (**2a**) (90% yield calculated by UV-vis spectroscopy) (Scheme 5); the same redox reaction is also observed with the authentic ferryl-oxo complex, as determined in a separate 'control' experiment, (b) the addition of triphenylphosphine to the reaction solution led to triphenylphosphine oxide, also a criterion used to demonstrate the presence of a ferryl ($Fe^{IV}{=}O$) species.[86]

To confirm the electron and proton transfer from the phenol to **2b** and the formation of the phenoxyl radical prior to the phenol coupling, we used 2,4,6-tri-*tert*-butylphenol and the 2,6-di-*tert*-buyl-4-methoxyphenol (Scheme 6), two phenols known to form relatively stable and detectable phenoxyl radicals.[87-89] The reaction of EPR-silent **2b** with those phenols in THF at -80° C leads to the formation of phenoxyl radical which displays an intense and characteristic EPR signal at 2.006 in the case of 2,4,6-tri-*tert*-butylphenol and at 2.008 in the case of 2,6-di-*tert*-buyl-4-methoxyphenol (Figure 11).

Summary & Perspectives

Our investigation into the nature of heme-peroxo-copper complexes has revealed that the denticity (tri- vs. tetradentate) of the copper ligand can have major influence on the molecular structure and the electronic-structure/bonding in such species. Using rR and EXAFS spectroscopic analyses coupled to DFT calculations, we have previously established a $\mu\text{-}(O_2^{2-})$ side-on to the Fe^{III} ion and end-on to Cu^{II} (i.e., $\mu\text{-}\eta^2{:}\eta^1$-peroxo) center binding in the

complex with tetradentate copper ligand $[(F_8)Fe^{III}\text{-}(O_2^{2-})\text{-}Cu^{II}(TMPA)]^+$ (**1**). However, in new investigations described here, side-on/side-on ($\mu\text{-}\eta^2\text{:}\eta^2$) μ-peroxo coordination for the complex with tridentate copper ligand is established for $[(F_8)Fe^{III}\text{-}(O_2^{2-})\text{-}Cu^{II}(AN)]^+$ (**2**). Insights into the electronic-structure/bonding of **2** and comparisons to **1** are described. A structural difference, for tridentate *versus* tetradentate copper ligand, was also directly observed by comparison of the X-ray structures of the μ-oxo complexes $[(F_8)Fe^{III}\text{-}(O^{2-}\text{-}Cu^{II}(TMPA)]^+$ (**1a**) and newly reported species $[(F_8)Fe^{III}\text{-}(O^{2-}\text{-}Cu^{II}(AN)]$ (**2a**), these obtained respectively by thermal decomposition of **1** and **2**.

These electronic and structural differences between the two dioxygen adducts result in a difference in their reactivity toward substrates such as CO or PPh_3. More interestingly, the difference between the two high-spin heme-peroxo complexes **1** and **2** is the ability of the latter with tridentate copper ligand to form a new low temperature stable low-spin complex [DCHIm $(F_8)Fe^{III}\text{-}(O_2^{2-})\text{-}Cu^{II}(AN)]^+$ (**2b**) in the presence of an axial base, tentatively assigned as a peroxo complex. Under the same conditions, complex **1** (tetradentate copper ligand) reacts with DCHIm only to break apart the heme-peroxo-copper assembly, essentially reversing its formation and releasing O_2.

In this study, we have also shown that in contrast to the behavior of the high-spin complexes **1** and **2**, the new low-spin complex **2b** reacts with phenols performing O-O bond cleavage which is accompanied by formation of the high valent ferryl heme species [DCHIm(F_8) Fe^{IV}=O] (**2c**).[77] This reaction occurs as a net hydrogen atom abstraction ($H^+ + e^-$) from the phenol with generation of a phenoxyl radical.

Given the new reactivity demonstrated by the low-spin complex, considerable future efforts are needed to determine the geometric and electronic structure of the low-spin system in comparison to the structure of high-spin system determined here. Such comparisons can contribute to a better understanding of the differenential reactivity observed dependent on the spin state in addition to different peroxo bridging modes. It is intruiging to consider if a bridging peroxo species could be identified as a fleeting intermediate in cytochrome *c* oxidase, would its spin state also be of central importance? Based on chemical precedent, and given the proximal histidine present in heme-copper oxidase enzymes, one would surmise a low-spin state was at work. Nonetheless, previous studies have suggested heme a_3 proximal histidine dissociation from iron, a mechanism which is known to occur in the evolutionarily related heme/non-heme diiron NO reductases, suggestive of a high-spin oxidant.

However, in addition to the spin state contribution to the O—O bond cleavage in heme-copper oxidases, proton and electron transport must also be considered. The order in which protons and electrons enter catalysis may shed light on the nature of the active oxidant. Our interest is especially piqued by the speculation of a discreet hydroperoxo species (either Cu or Fe bound, or both), given the generality of such a potential reaction. As such we have embarked on studies, some of which are alluded to herein, to test the possibility of such species and their respective reactivity for insight into the mechanism of heme-copper oxidases.

Within the context of 1) the nature of the active oxidant and 2) the role of protons and electrons in driving a particular reaction coordinate, the issue of the active site tyrosine remains intruiging to us from a mechanistic standpoint. While it is generally accepted that a tyrosine radical forms at some point during the reaction, it remains an open question as to when its proton and electron enter the catalytic cycle and by what means. Specifically, 1) does the active site oxidant do direct H-atom abstraction from the tyrosine, or does the reaction occur stepwise, and 2) do the transfers occur before or after the O—O bond is cleaved. Stepwise mechanisms would indicate the importance of the Tyr-His crosslink to form an adequate superexchange pathway for electron transfer and would significantly enhance the functional role of copper in mediating

the electron transfer. Finally, how would such a crosslink be formed in an active site? Presumably one would invoke some sort of oxidative coupling involving reduced oxygen species in the proenzyme before the first turnover (the cofactor biogenesis reaction), but would that process require both copper and iron? Hopefully, our foray into small molecule analogs as probes of these potential mechanistic scenarios continues to shed light on these critical questions, given the enormous scope of the processes involved and applicability to problems ranging from disease to energy conversion.

Experimental Section

Materials and Methods

All reagents and solvents were purchased from commercial sources and were of reagent quality unless otherwise noted. Tetrahydrofuran (THF) was distilled from sodium/benzophenone under argon, and acetonitrile (CH_3CN) was purified over and activated alumina column. Preparation and handling of air-sensitive compounds were performed under MBraun Labmaster 130 inert atmosphere (<1 ppm O_2, <1 ppm H_2O) glove box filled with nitrogen. Deoxygenation of solvents was effected either by repeated freeze/pump/thaw cycles of by bubbling with argon for 30-45 min.

Low-temperature UV-vis Low-temperature UV-vis spectra were recorded on a Hewlett-Packard Model 8453A diode array spectrometer with HP Chemstation software; the instrument was equipped with a variable-temperature Dewar and cuvette. ^1H and ^2H NMR spectra were measured on a Varian XL-400 NMR instrument and Bruker 400 MHz spectrometer at ambient or a low temperatures. All spectra were recorded in 5 mm o.d. NMR tubes, and chemical shifts δ (ppm) were referenced either to an internal standard (Me_4Si) or to residual solvent peaks. Electron paramagnetic resonance (EPR) spectra were obtained in frozen solutions with 4 mm o.d. quartz tubes in a Bruker EMX spectrometer operating at X-band using microwave frequencies around 9.5 GHz, with sample temperature maintained at 77 K. EPR spectra were referenced to 2,2-diphenyl-1-picrylhydrazyl (g = 2.0036). Elemental analyses were performed by Desert Analytics (Tuscon, AZ). The coupled phenol was analyzed by gas chromatography-mass spectrometry (GC-MA) on a Shimadzu GC17A/QP5050A instrument equipped with a non-polar column (DB-5 ms). Helium was used as the carrier gas at a flow rate of 27 cm s^{-1}. Injections were made in split mode using an initial column temperature of 100° C. The temperature was raised by 20° C per min to 300° C with an initial and final hold time of 3 min and 2 min.

XAS Data Acquisition

The Cu and Fe K-edge X-ray absorption spectra of $[(F_8)Fe^{III}\text{-}O_2\text{-}Cu^{II}(AN)](ClO_4)$ in solution form were measured at the Stanford Synchrotron Radiation Lightsource (SSRL) on the focused 16-pole, 2.0-T wiggler beam line 9-3 under storage ring parameters of 3 GeV and 80-100 mA. A Rh-coated premonochromator flat bent mirror was used for harmonic rejection and vertical collimation, while a bent cylindrical Rh-coated post-monochromator mirror was used for focusing. A Si(220) double crystal monochromator was used for energy selection. ~150 μL of the solution samples were loaded into 2 mm Delrin XAS cells with a 38 μm Kapton window. The samples were immediately frozen and stored under liquid nitrogen. The samples were maintained at a constant temperature of ~10 K during data collection using an Oxford Instruments CF 1208 continuous-flow liquid helium cryostat. A Canberra solid-state Ge 30-element array detector was used to collect Kα fluorescence data. Data reported here are up to $k = 12.8$ Å^{-1} for Cu in order to avoid interference from the Zn K-edge, and up to $k = 16$ Å^{-1} for Fe. Internal energy calibration was performed by simultaneous measurement of the absorption of the corresponding metal foil placed between two ionization chambers located after the sample. The first inflection point of the foil spectrum was assigned to 8980.3 eV for Cu and

7111.2 eV for Fe. To reduce photoreduction, data were collected on four distinct and physically separate spots, two spots for Cu and two spots for Fe. A total of 12 and 19 scans were measured at the Cu and Fe K-edge respectively with no significant change from photoreduction observed.

XAS Data Analysis

The energy-calibrated averaged data were processed by fitting a second-order polynomial to the pre-edge region and subtracting this from the entire spectrum as a background. A three-region spline of orders 2, 3, and 3 was used to model the smoothly decaying post-edge region. The data were normalized by scaling the spline function to an edge jump of 1.0 at 9000 eV for Cu and 7130 for Fe. This background subtraction and normalization was done using PySpline.[92] The least-squares fitting program OPT in EXAFSPAK[93] was used to fit the data. Initial ab initio theoretical phase and amplitude functions were generated in FEFF 7.0[94] using crystallographic parameters of the oxo complex $[(F_8)Fe\text{-}O\text{-}Cu\ (AN)]^+$ as the starting model. The final model used was based on the DFT optimized structure. Atomic coordinates were further adjusted as necessary as fits were improved. During the fitting process, the bond distance (R), and the mean-square thermal and static deviation in R (σ^2) were varied for all components. The threshold energy (ΔE_0) was also allowed to vary for each fit but was constrained to the same value for all components in a given fit. Coordination numbers (N) were systematically varied to provide the best chemically viable agreement to the EXAFS data and Fourier transform but was fixed within a given fit.

Resonance Raman

Samples were prepared as previously described as 1mM THF solutions in NMR tubes. Samples were excited at 413 nm using a Coherent I90C-K Kr+ ion laser while the sample was immersed in a liquid nitrogen cooled (77 K) EPR finger dewar (Wilmad). Power was 2 mW at the sample. Data were recorded while rotating the sample to minimize photodecomposition. The spectra were recorded using a Spex 1877 CP triple monochromator with a 1200 groves/mm holographic spectrograph grating, and an Andor Newton CCD cooled to -80° C. Spectra were calibrated to toluene.

Computational methods

Density functional calculations were performed using Gaussian03.[95] Models of **1** and **2** and were constructed based loosely on crystallographically derived parameters of the monometallic molecular fragments. Calculations were performed with the BP86 functional within the unrestricted formalism (B3LYP incorrectly predicts the ground state as HS ($S = 3$), and a previous assessment of functional dependence for the truncated $[(P)Fe\text{-}O\text{-}Cu(AN)]^+$ complex supports the choice of the BP86 functional). A triple-ζ basis set with polarization (6-311G*) was used on the Cu, Fe, and O_2. A split-valence basis (6-31G) was used on all remaining atoms (F, C, H), supplemented by polarization functions in the case of N (6-31g*). Density fitting was employed and models were optimized to default convergence criteria (unless otherwise noted) on ultrafine integration grids. Models were first subjected to a coarse optimization on the high-spin ($S_T = 3$) surface, followed by a single point calculation to obtain a spin-polarized broken-symmetry solution. The models were then reoptimized on the BS ($S_T = 2$) surface to yield final atomic coordinates. Analytical frequency calculations were performed to ensure stationary points on the models' respective potential energy surfaces had been reached. No imaginary frequencies were obtained. Mulliken population analysis was performed with QMForge.[96]

Generation of $[(F_8)Fe\text{-}(O^{2-})\text{-}Cu(AN)]^+$ BArF- (2a)

In a 100 mL Schlenk flask equipped with a stir bar were placed, in the drybox, 210 mg (0.2 mmol) of $(F_8)Fe^{II}$ and 186 mg (0.2 mmol, 1.0 equiv.) of $[(AN)Cu^{I}](BArF)$, to which was added

air-free freshly distilled THF (20 mL). The reaction mixture was cooled to -80° C (dry ice-acetone bath) and stirred for 30 min. The solution was subject to O_2 purging and finally allowed to warm slowly at room temperature and then layered with 50 mL of deoxygenated heptane. After 12 h, the solution was filtered and the black microcrystalline solid dried in vacuo (245 mg, 70% yield). Anal. Calcd. (found): C, 53.28 (53.22); H, 2.58 (2.59); N, 5.58 (5.63). ^{1åå}H NMR (CD_2Cl_2): δ (s, 8H, pyrrole), 9.8-9.14 (d, 8H, m-phenyl), 7.67-7.51 (m, 16H, 8H BArF + p-phenyl); UV-visible (CH_2Cl_2): 440, 557 nm.

Generation and Characterization of [(DCHIm)(F_8)Fe^{III}-(O_2^{2-})-Cu^{II}(AN)]$^+$ (2b)

(a) UV-vis Spectroscopy—[(F_8)Fe^{III}-(O_2^{2-})-Cu^{II}(AN)]$^+$ (**2**) was synthesized as previously reported.[37] To 4 mL of 0.36 mM THF solution of dioxygen adduct (**2**), 1.0 equiv. (100 μL of 14.4 mM, 0.30 mg) of DCHIm was added to generate low spin [(DCHIm)(F_8)Fe^{III}-(O_2^{2-})-Cu^{II}(AN)]$^+$ which was characterized by UV-vis spectra [λ_{max} (ε, $mM^{-1}cm^{-1}$) = 421 (soret: 146.5), 537 (8.2) nm]. Upon warming up the solution leads to the formation of hydroxo complex [(F_8)Fe^{III}-OH] with λ_{max} (ε, $mM^{-1}cm^{-1}$) at 412 (156.3) and 572 nm (9.3).

(b) ^{2}H NMR Spectroscopy—In the glovebox, 1:1 mixture of (d^8-F_8)Fe^{II}.H_2O (3.0 mg, 3.5 mM) and [Cu^I(AN)]$^+$ (3.32 mg, 3.5mM) was taken in 5 mm NMR tube and dissolved in 0.5 mL of THF. To the cold THF solution (at – 80° C, dry ice – acetone) of (d^8-F_8)Fe^{II}.H_2O and [Cu^I(AN)]$^+$, 2 mL of O_2 was bubbled and the NMR was recorded at -80° C. A peak at 96 ppm was observed as reported previously, corresponds to the chemical shift of pyrrole deuterium atoms of [(d^8F_8)Fe^{III}-(O_2^{2-})-Cu^{II}(AN)]$^+$. To the same NMR tube 1.5 equiv. (1.2 mg of DCHIm in 0.05 mL of THF) of DCHIm was added, new peak at upfield 8.31 ppm was observed.

UV-vis spectroscopy monitoring of the reaction of [(F_8)Fe^{III}-(O_2^{2-})-Cu^{II}(TMPA)]$^+$ (1) with axial ligand bases

In a modified low-temperature cuvette assembly equipped with a Schlenk-type sidearm, a solution of (**1**) was generated in CH_3CN at – 40° C as previously described.[37] A stock solution of equimolar amounts of (F_8)Fe^{II}•H_2O (13 mg) and [Cu^I(TMPA)(CH_3CN)](ClO_4) (8 mg) in 6 g deoxygenated CH_3CN is prepared in glovebox and 0.3 g of stock solution is diluted to 10 g and transferred to the UV-vis cuvette. Generation of the peroxo adduct (λ_{max} = 558, 535 (sh) nm) is accomplished by bubbling excess dioxygen to the solution at -40° C. Removal of excess O_2 is performed by application of 3-5 vacuum/Ar cycles. Then 1, 3 and 5 equiv of 4-(dimethylamino)pyridine (DMAP) (50, 150 and 250 μl respectively of DMAP stock solution prepared with 19.5 mg DMAP in 10 ml CH_3CN) were added and the respective spectra recorded at – 40° C (see Figure S2). The new Q-band spectral feature (λ_{max} = 527 nm) is assigned to the formation of (F_8)Fe^{II}(DMAP)$_2$. A control experiment by addition of DMAP to a solution of the mixture of (F_8)Fe^{II}/[Cu^I(TMPA)(CH_3CN]$^+$ yielded the same spectrum. The experiment was repeated in the non-polar solvent CH_2Cl_2 (instead of CH_3CN) and also using 1,5-(dicyclohexyl)imidazole (DCHIm) as axial ligand base (instead of DMAP) in CH_3CN, and the results were essentially the same in both cases.

Reaction of [(F_8)Fe^{III}-(O_2^{2-})-Cu^{II}(TMPA)]$^+$ (1) with DMAP – Determination of dioxygen evolution

Dioxygen evolution was quantitatively determined using an alkaline pyrogallol solution (1,2,3-trihydroxybenzene), following a methodology used frequently in our laboratory.[29,37] In the glovebox, equimolar amounts of (F_8)Fe^{II}•H_2O (40 mg) and [Cu^I(TMPA)(CH_3CN)](ClO_4) (24 mg) were dissolved in 10 ml of deoxygenated CH_3CN, transferred to a 50 ml Schlenk flask with a stir-bar and capped with a rubber septum. The flask was taken out of the glovebox, the solution was cooled down to –40° C (adding dry ice to acetone bath, temperature followed by thermocouple), and then O_2 was gently bubbled into the solution using a syringe with long

needle. To ensure complete formation of the peroxo compound, the solution was allowed to stand in the cold bath for 30 minutes. Excess/free O_2 is removed via 5 freeze-pump-thaw cycles. In parallel with the reaction, 4.0 g of pyrogallol were dissolved in 25 ml of deoxygenated 50% KOH solution in a specially designed 100 ml Schlenk flask possessing a 2 mm path length cuvette; its UV-vis spectrum was recorded. Excess DMAP (10 equiv.: 1 ml solution prepared with 293 mg DMAP in 5 ml CH_3CN) was added to the peroxo adduct solution thus allowing O_2 release. The O_2 was then moved from the reaction flask to the pyrogallol flask by passing slowly argon through the headspace of the reaction flask thus moving the O_2 through a cannula to the pyrogallol flask. The O_2 was then bubbled directly into the pyrogallol solution whose color changed from faint beige to dark brown after some minutes. After 20-30 minutes, the pyrogallol solution ceased becoming darker and its UV-vis spectrum was recorded. The amount of O_2 released was determined using a calibration curve where absorbance (400 nm) = (0.0716 × mL O_2) + 0.025.[29] Based on the stoichiometry of the reaction where 1 equiv. of peroxo compound decomposes to give 1 equiv. of O_2, two experiments yielded 90 and 91% O_2 detection.

Reaction of $[(F_8)Fe^{III}\text{-}(O_2^{2-})\text{-}Cu^{II}(TMPA)]^+$ (1) with DMAP – Characterization of the product $(F_8)Fe^{II}(DMAP)_2$

In the same experiment described above, $(F_8)Fe^{II}(DMAP)_2$ precipitated spontaneously and was isolated by filtration under argon, washed, vacuum-dried for 2 hours and finally stored in glove box. Yield was 70 %. The purple solid was characterized by elemental analysis consistent with a formulation as monohydrate solid, $(F_8)Fe^{II}(DMAP)_2.H_2O$, *Desert Analytics*, $C_{58}H_{42}N_8F_8FeO$ found/calc: %C 64.5/64.8; %H 3.6/3.9; %N 10.1/10.4; UV-vis (CH_3CN, 293 K) λ_{max} = 418.5 nm (Soret), 527 nm (Q-band); ^{1}H-NMR showing a typical spectrum of low-spin iron(II) porphyrin, 400 MHz, CD_2Cl_2, 300 K, δ (ppm) = 7.6 (pyrrole-H); 7.2 (phenyl-H); 1.5 (H_2O); MALDI-TOF mass spectrum shows a peak characteristic of the monobase $(F_8)Fe^{II}(DMAP)$ (probably the other base is lost by effect of the laser): [M – DMAP – H_2O] *m/z* = 935, [M – 2 DMAP – H_2O] *m/z* = 812.

UV-vis spectroscopy monitoring of the reaction of $[DCHIm(F_8)Fe^{III}\text{-}(O_2^{2-})\text{-}Cu^{II}(AN)]^+$ (2b) with 2,4-di-tert-butylphenol

In a UV-vis cuvette assembly, a solution of $[(DCHIm)(F_8)Fe^{III}\text{-}(O_2^{2-})\text{-}Cu^{II}(AN)]^+$ (0.36 mM) was generated in THF at –80° C as described above; 1.0 equiv of 2,4-di-*tert*-butylphenol (0.29 mg, 14.4 mM) was then added. UV-vis absorption at λ_{max} (ε, $mM^{-1}cm^{-1}$) = 419 (Soret: 133.8), 541 (8.5) nm] corresponds to high-valent oxyferryl $[(DCHIm)(F_8)Fe^{IV}{=}O]$ (spectra are given in Supporting Information, Figure S1).

Reactivity of $[DCHIm(F_8)Fe^{III}\text{-}(O_2^{2-})\text{-}Cu^{II}(AN)]^+$ (2b) in presence of HCl and quantitive determination of H_2O_2

Equimolar amounts of $(F_8)Fe^{II}{\cdot}H_2O$ (20 mg) and $[Cu^I(AN)(CH_3CN)]ClO_4$ (9.8 mg) were dissolved in 10 mL of CH_3CN (conc = 3 mM) in the glovebox. The solution was brought out of the glovebox and immersed in a cold bath at − 40° C, and dioxygen was then bubbled through the solution to generate the high-spin peroxo compound **2a**. Excess O_2 was removed by several vacuum/Ar cycles; then 1.0 equiv. of 1,5-dicyclohexylimidazole (DCHIm) (5.6 mg in 0.1 mL of CH_3CN) was added to form the low-spin peroxo complex **2b**. 10 equiv. of HCl (0.24 mL of 1.0 M diethyl ether solution of hydrogen chloride, Aldrich) was added, and the dark red solution turned to dark green. The solution was removed from the cold bath, followed by addition of 20 mL of distilled water (final volume = 30.3 mL). A suspension is formed because of the insolubility of $(F_8)Fe^{III}$–Cl in the solvent mixture. H_2O_2 was determined spectrophotometrically (at 408 nm) upon addition of 1 mL of titanyl reagent (titanium(IV) oxysulfate in sulfuric acid, Riedel de Haën) to a 10 mL suspension, followed by centrifugation.

A calibration curve was made in the same solvent mixture of the reaction (CH_3CN/Ether/H_2O). The yield of H_2O_2 was determined to be 70% on the basis of two experiments.

UV-vis spectroscopy monitoring of the reaction of [(DCHIm)(F_8)Fe^{IV}=O] (1c) with [Cu^{I}(AN)][$B(C_6F_5)_4$]

To the UV-vis cuvette containing THF solution of [(DCHIm)(F_8)Fe^{IV}=O] (prepared by reaction of (**2b**) with 2,4-di-tert-butylphenol. as discussed above, 1.0 equiv. of $[Cu^{I}(AN)]^+$ (1.33 mg in 0.1 mL in THF) at – 80° C. UV-vis absorption at λ_{max} 440, 553 nm corresponds to $[(F_8)Fe^{III}\text{-}(O^{2-})\text{-}Cu^{II}(AN)]^+$.

EPR spectroscopy Identification of $[Cu^{II}(AN)(OH)]^+$ as product of the reaction of [(DCHIm)(F_8)Fe^{III}-(O_2^{2-})-Cu^{II}(AN)]$^+$ (2b) with 2,4-di-*tert*-butyl phenol

In the glove box, 1.6 mg of $(F_8)Fe^{II}.H_2O$ and 1.8 mg of $[Cu^{I}(AN)]^+$ is dissolved in 0.4 mL of deoxygenated acetone in a EPR tube. Outside the glovebox, the solution was cooled to -80° C (acetone/dry ice bath) and bubbled with dioxygen to generate the peroxo compound (**2b**). 1 equiv. of DCHIm (50 μL of 40 mM acetone solution of DCHIm) was added to the reaction mixture followed by addition of 50 μL of 40 mM acetone solution of 2,4-di-*tert*-butylphenol (1 equiv.). Then, the EPR spectrum was recorded at 77 K. [EPR parameters $A_{\parallel} = 127.33 \times 10^{-4}$ cm^{-1}, $A_{\perp} = 35 \times 10^{-4}$ cm^{-1}, $g_{\parallel} = 2.24$ and $g_{\perp} = 2.06$]. The solution was warmed up to room temperature, and again an EPR spectrum was recorded at 77 K. The thermally decomposed products [(F_8)Fe^{III}–OH] (g = 5.8) and $[Cu^{II}(AN)(OH)]^+$ were formed (spectra are given Supporting Information, Figure S3).

Identification and quantification of coupled phenol (3,3',5,5'-tetra-tert-butyl-(1,1'-biphenyl)-2,2'-diol) by GC-MS

In the glove box, 16.6 mg of $(F_8)Fe^{II}.H_2O$ and 18.5 mg of $[Cu^{I}(AN)]^+$ was dissolved in 2 mL of THF in a Schlenk flask. Outsied the glovebox, the solution was cooled to -80 °C and bubbled with dioxygen to generate the peroxo adduct. The excess dioxygen was removed by employing vacuum and Argon bubbling through the solution for 2 cycles. To the solution, 4.6 mg of DCHIm in 0.2 mL of THF (1 equiv.) was added, followed by addition 1 equiv. of 2,4-di-*tert*-butylphenol (4.6 mg of phenol in 0.4 mL of THF). Then the solution was stirred for 2 hrs and warmed up to RT. The volume of the solution was reduced to 0.5 mL and the metal complexes are precipitated by the addition of 10 mL of pentane, and separated by filtration. The filterate was carefully collected and pentane was removed by vacuum, the organic residue was redissolved in 4 mL of CH_3CN. The coupled phenol generated in this reaction was quantitatively determined by GC-MS. Yield of 3,3',5,5'-tetra-*tert*-butyl-(1,1'-biphenyl)-2,2'-diol is 68.5 % (GC-MS trace is given in Supporting Information, Figure S4).

Identification of 2,4,6-tri-tert-butylphenoxy radical and 2,4-di-*tert*-butyl-4-methoxylphenoxy radical by EPR spectroscopy

This reaction was carried out in a manner similar to that described above except that either 2,4,6-tri-*tert*-butylphenol or 2,4-di-*tert*-butyl-4-methoxylphenol was used. Then, the EPR spectrum was recorded at 77 K, g value for 2,4,6-tri-*tert*-butylphenoxy radical and 2,4-di-*tert*-butyl-4-methoxylphenoxy radical are 2.0056 and 2.0077 respectively.

Supplementary Material

Refer to Web version on PubMed Central for supplementary material.

Acknowledgments

These studies were supported in part by the NIH (DK031450 E.I.S.; RR-001208 K.O.H.. Computational resources used in these studies were provided in part by the Bioinformatics Center of the University of Arkansas for Medical Sciences (NIH P20 RR-16460 from the IDeA Networks of Biomedical Research Excellence (INBRE) Program of the National Center for Research Resources) and in part by the National Science Foundation through TeraGrid resources provided by the NCSA (TG-CHE080054N). K.D.K. acknowledges support from the NIH (GM60353) and WCU-Program R31-2008-000-10010-0. The XAS data were measured at SSRL, the operations of which is funded by the Department of Energy, Office of Basic Energy Sciences. The SSRL Structural Molecular Biology program is supported by the National Institutes of Health, National Center for Research Resources, Biomedical Technology Program and by the Department of Energy, Office of Biological and Environmental Research. This publication was made possible by Grant Number 5 P41 RR001209 from the National Center for Research Resources (NCRR), a component of the National Institutes of Health (NIH). Its contents are solely the responsibility of the authors and do not necessarily represent the official view of NCRR or NIH.

References

1. Ferguson-Miller S, Babcock GT. Chem. Rev 1996;96:2889–2907. [PubMed: 11848844]
2. Iwata S, Ostermeier C, Ludwig B, Michel H. Nature 1995;376:660–669. [PubMed: 7651515]
3. Yoshikawa S, Shinzawa-Itoh K, Nakashima R, Yaono R, Yamashita E, Inoue N, Yao M, Jei-Fei M, Libeu CP, Mizushima T, Yamaguchi H, Tomizaki T, Tsukihara T. Science 1998;280:1723–1729. [PubMed: 9624044]
4. Kim E, Chufán EE, Kamaraj K, Karlin KD. Chem. Rev 2004;104:1077–1133. [PubMed: 14871150]
5. Collman JP, Boulatov R, Sunderland CJ, Fu L. Chem. Rev 2004;104:561–588. [PubMed: 14871135]
6. Chufán EE, Puiu SC, Karlin KD. Acc. Chem. Res 2007;40:563–572. [PubMed: 17550225]
7. Blomberg LM, Blomberg MRA, Siegbahn PEM. J. Inorg. Biochem 2005;99:949–958. [PubMed: 15811512]
8. de Vries S. Biochimica et Biophysica Acta (BBA) - Bioenergetics 2008;1777:925–928.
9. Proshlyakov DA, Pressler MA, Babcock GT. Proc. Natl. Acad. Sci. USA 1998;95:8020–8025. [PubMed: 9653133]
10. Blomberg MRA, Siegbahn PEM, Wikström M. Inorg, Chem 2003;42:5231–5243. [PubMed: 12924894]
11. Ogura T, Kitagawa T. Biochim. Biophys. Acta 2004;1655:290–297. [PubMed: 15100044]
12. Blomberg MRA, Siegbahn PEM. Biochim. Biophys. Acta 2006;1757:969–980. [PubMed: 16483535]
13. Himo F, Siegbahn PEM. Chem. Rev 2003;103:2421–2456. [PubMed: 12797836]
14. Huynh MHV, Meyer TJ. Chem. Rev 2007;107:5004–5064. [PubMed: 17999556]
15. Yoshioka Y, Satoh H, Mitani M. J. Inorg. Biochem 2007;101:1410–1427. [PubMed: 17662458]
16. Karlin KD. Science 1993;261:701–708. [PubMed: 7688141]
17. Holm RH, Solomon EI. Biomimetic Inorganic Chemistry. Chem. Rev 2004;104(2)
18. Lee, Y.; Karlin, KD. Highlights of Copper Protein Active-Site Structure/Reactivity and Synthetic Model Studies. In: Metzler-Nolte, N.; Kraatz, H-B., editors. Concepts and Models in Bioinorganic Chemistry. Wiley-VCH; New York: 2006. p. 363-395.
19. Collman JP, Decréau RA. Chem. Commun 2008:5065–5076.
20. Liu JG, Naruta Y, Tani F. Angew. Chem. Int. Ed 2005;44:1836–1840.
21. Liu J-G, Naruta Y, Tani F. Chem. Eur. J 2007;13:6365–6378.
22. Collman JP, Devaraj NK, Decreau RA, Yang Y, Yan Y-L, Ebina W, Eberspacher TA, Chidsey CED. Science 2007;315:1565–1568. [PubMed: 17363671]
23. Bröring M. Angew. Chem. Int. Ed 2007;46:6222–6224.
24. Ghiladi RA, Hatwell KR, Karlin KD, Huang H.-w. Moënne-Loccoz P, Krebs C, Huynh BH, Marzilli LA, Cotter RJ, Kaderli S, Zuberbühler AD. J. Am. Chem. Soc 2001;123:6183–6184. [PubMed: 11414855]
25. del Rio D, Sarangi R, Chufán EE, Karlin KD, Hedman B, Hodgson KO, Solomon EI. J. Am. Chem. Soc 2005;127:11969–11978. [PubMed: 16117536]

26. Ghiladi RA, Chufan EE, del Rio D, Solomon EI, Krebs C, Huynh BH, Huang H. w. Moenne-Loccoz P, Kaderli S, Honecker M, Zuberbuhler AD, Marzilli L, Cotter RJ, Karlin KD. Inorg. Chem 2007;46:3889–3902. [PubMed: 17444630]
27. Chishiro T, Shimazaki Y, Tani F, Tachi Y, Naruta Y, Karasawa S, Hayami S, Maeda Y. Angew. Chem. Int. Ed 2003;42:2788–2791.
28. Ghiladi RA, Ju TD, Lee D-H, Moënne-Loccoz P, Kaderli S, Neuhold Y-M, Zuberbühler AD, Woods AS, Cotter RJ, Karlin KD. J. Am. Chem. Soc 1999;121:9885–9886.
29. Ghiladi RA, Huang HW, Moënne-Loccoz P, Stasser J, Blackburn NJ, Woods AS, Cotter RJ, Incarvito CD, Rheingold AL, Karlin KD. J. Biol. Inorg. Chem 2005;10:63–77. [PubMed: 15583964]
30. Kim E, Kamaraj K, Galliker B, Rubie ND, Moënne-Loccoz P, Kaderli S, Zuberbühler AD, Karlin KD. Inorg. Chem 2005;44:1238–1247. [PubMed: 15732964]
31. Hatcher LQ, Karlin KD. Adv. Inorg. Chem 2006;58:131–184.
32. Hatcher LQ, Karlin KD. J. Biol. Inorg. Chem 2004;9:669–683. [PubMed: 15311336]
33. Mirica LM, Ottenwaelder X, Stack TDP. Chem. Rev 2004;104:1013–1045. [PubMed: 14871148]
34. Ross PK, Solomon EI. J. Am. Chem. Soc 1991;113:3246–3259.
35. Ross PK, Solomon EI. J. Am. Chem. Soc 1990;112:5871–5872.
36. Solomon EI, Tuczek F, Root DE, Brown CA. Chem. Rev 1994;94:827–856.
37. Chufan EE, Mondal B, Gandhi T, Kim E, Rubie ND, Moenne-Loccoz P, Karlin KD. Inorg. Chem 2007;46:6382–6394. [PubMed: 17616124]
38. Kim E, Helton ME, Wasser IM, Karlin KD, Lu S, Huang H.-w. Moënne-Loccoz P, Incarvito CD, Rheingold AL, Honecker M, Kaderli S, Zuberbühler AD. Proc. Natl. Acad. Sci. USA 2003;100:3623–3628. [PubMed: 12655050]
39. Kim E, Helton ME, Lu S, Moënne-Loccoz P, Incarvito CD, Rheingold AL, Kaderli S, Zuberbühler AD, Karlin KD. Inorg, Chem 2005;44:7014–7029. [PubMed: 16180864]
40. Kim E, Shearer J, Lu S, Moënne-Loccoz P, Helton ME, Kaderli S, Zuberbühler AD, Karlin KD. J. Am. Chem. Soc 2004;126:12716–12717. [PubMed: 15469233]
41. Ghiladi RA, Kretzer RM, Guzei I, Rheingold AL, Neuhold Y-M, Hatwell KR, Zuberbühler AD, Karlin KD. Inorg. Chem 2001;40:5754–5767. [PubMed: 11681882]
42. The EXAFS envelopes obtained from a single scatterer (SS) with atomic number Z and Z±1 at the same distance from the absorber are indistinguishable. Ths, Cu-O/N refers to a single scattering contribution from either O or N.
43. Cu-O-Fe = $\cos^{-1}\{[(\text{Cu-O})^2+(\text{Fe-O})^2-(\text{Cu-Fe})^2]/2(\text{Cu-O})(\text{Fe-O})\}$
44. Wasser IM, Huang HW, Moenne-Loccoz P, Karlin KD. J. Am. Chem. Soc 2005;127:3310–3320. [PubMed: 15755147]
45. We use the “holes” here to reflect uncompensated occupied valence orbitals; the Cu(II) has negative spin density and the Fe(III) has positive spin density,
46. Chen P, Fujisawa K, Helton ME, Karlin KD, Solomon EI. J. Am Chem. Soc 2003;125:6394–6408. [PubMed: 12785779]
47. Henson MJ, Mahadevan V, Stack TDP, Solomon EI. Inorg. Chem 2001;40:5068–5069. [PubMed: 11559060]
48. Chufán EE, Karlin KD. J. Am Chem. Soc 2003;125:16160–16161. [PubMed: 14692736]
49. Karlin KD, Nanthakumar A, Fox S, Murthy NN, Ravi N, Huynh BH, Orosz RD, Day EP. J. Am. Chem. Soc 1994;116:4753–4763.
50. Fox S, Nanthakumar A, Wikström M, Karlin KD, Blackburn NJ. J. Am. Chem. Soc 1996;118:24–34.
51. Du Bois J, Mizoguchi TJ, Lippard SJ. Coord. Chem. Rev 2000;200-202:443–485.
52. Feig, a. L.; Becker, M.; Schindler, S.; van Eldik, F.; Lippard, SJ. Inorg. Chem 2003;42:3704–3704.
53. Scheidt WR, Reed CA. Chem. Rev 1981;81:543–555.
54. Obias HV, van Strijdonck GPF, Lee D-H, Ralle M, Blackburn NJ, Karlin KD. J. Am. Chem. Soc 1998;120:9696–9697.
55. Kurtz DM Jr. Chem. Rev 1990;90:585–606.
56. Que L Jr. Tolman WB. Angew. Chem. Int. Ed 2002;41:1114–1137.

57. Yeh C-Y, Chang CJ, Nocera DG. J. Am. Chem. Soc 2001;123:1513–1514. [PubMed: 11456732]
58. Scott MJ, Zhang HH, Lee SC, Hedman B, Hodgson KO, Holm RH. J. Am. Chem. Soc 1995;117:568–569.
59. Lee SC, Holm RH. Inorg. Chem 1993;32:4745–4753.
60. Koval IA, van der Schilden K, Schuitema AM, Gamez P, Belle C, Pierre JL, Luken M, Krebs B, Roubeau O, Reedijk J. Inorg. Chem 2005;44:4372–4382. [PubMed: 15934768]
61. Mahapatra S, Halfen JA, Wilkinson EC, Pan G, Wang X, Young J,VG, Cramer CJ, Que J,L, Tolman WB. J. Am. Chem. Soc 1996;118:11555–11574.
62. Berreau LM, Mahapatra S, Halfen JA, Young VG, Tolman WB. Inorg. Chem 1996;35:6339–&.
63. Obias HV, Lin Y, Murthy NN, Pidcock E, Solomon EI, Ralle M, Blackburn NJ, Neuhold Y-M, Zuberbühler AD, Karlin KD. J. Am. Chem. Soc 1998;120:12960–12961.
64. Shearer J, Zhang CX, Zakharov LN, Rheingold AL, Karlin KD. J. Am. Chem. Soc 2005;127:5469–5483. [PubMed: 15826184]
65. Izzet G, Akdas H, Hucher N, Giorgi M, Prange T, Reinaud O. Inorg. Chem 2006;45:1069–1077. [PubMed: 16441115]
66. Hong S, Hill LMR, Gupta AK, Naab BD, Gilroy JB, Hicks RG, Cramer CJ, Tolman WB. Inorg. Chem 2009;48:4514–4523. [PubMed: 19425614]
67. Contaldi S, Nicola CD, Garau F, Karabach YY, Martins LMDRS, Monari M, Pandolfo L, Pettinari C, Pombeiro AJL. Dalton Trans 2009:4928–4941. [PubMed: 19662285]
68. Itoh S, Tachi Y. Dalton Trans 2006:4531–4538. [PubMed: 17016563]
69. Collman JP, Herrmann PC, Boitrel B, Zhang X, Eberspacher TA, Fu L, Wang J, Rousseau DL, Williams ER. J. Am. Chem. Soc 1994;116:9783–9784.
70. Collman JP, Fu L, Herrmann PC, Zhang X. Science 1997;275:949–951. [PubMed: 9020071]
71. Collman JP. Inorg. Chem 1997;36:5145–5155.
72. Collman JP, Fu L, Herrmann PC, Wang Z, Rapta M, Bröring M, Schwenninger R, Boitrel B. Angew. Chem. Int. Ed 1998;37:3397–3400.
73. Kim Y, Shinzawa-Itoh K, Yoshikawa S, Kitagawa T. J. Am. Chem. Soc 2001;123:757–758. [PubMed: 11456599]
74. Collman JP, Decréau RA, Sunderland CJ. Chem. Commun 2006:3894–3896.
75. Lehnert N, Ho RYN, Que L Jr. Solomon EI. J. Am Chem. Soc 2001;123:12802–12816. [PubMed: 11749538]
76. Lehnert N, Ho RYN, Que L Jr. Solomon EI. J. Am. Chem. Soc 2001;123:8271–8290. [PubMed: 11516278]
77. Experiments to assign the structure of 2b are in progress.
78. Balch AL. Inorg. Chim. Acta 1992;198-200:297–307.
79. Park GY, Deepalatha S, Puiu SC, Lee D-H, Mondal B, Narducci Sarjeant AA, del Rio D, Pau MYM, Solomon EI, Karlin KD. J. Biol. Inorg. Chem 2009;14:1301–1311. [PubMed: 19662443]
80. Paul PP, Tyeklár Z, Jacobson RR, Karlin KD. J. Am. Chem. Soc 1991;113:5322–5332.
81. Lucchese B, Humphreys KJ, Lee D-H, Incarvito CD, Sommer RD, Rheingold AL, Karlin KD. Inorg. Chem 2004;43:5987–5998. [PubMed: 15360248]
82. Halfen JA, Young VG Jr. Tolman WB. Inorg. Chem 1998;37:2102–2103. [PubMed: 11670360]
83. Mahadevan V, DuBois JL, Hedman B, Hodgson KO, Stack TDP. J. Am. Chem. Soc 1999;121:5583–5584.
84. Kushioka K. J. Org. Chem 1983;48:4948–4950.
85. Chin DH, Lamar GN, Balch AL. J. Am. Chem. Soc 1980;102:5945–5947.
86. Collman JP, Decreau RA, Yan Y, Yoon J, Solomon EI. J. Am. Chem. Soc 2007;129:5794–5795. [PubMed: 17429972]
87. Manner VW, Markle TF, Freudenthal JH, Roth JP, Mayer JM. Chem. Commun 2008:256–258.
88. Hicks RG. Org. Biomol. Chem 2007;5:1321–1338. [PubMed: 17464399]
89. Altwicker ER. Chem. Rev 1967;67:475.

90. Nakanishi I, Fukuhara K, Shimada T, Ohkubo K, Iizuka Y, Inami K, Mochizuki M, Urano S, Itoh S, Miyata N, Fukuzumi S. J Chem Soc Perk T 2 2002:1520–1524.
91. Yamaji T, Saiful ISM, Baba M, Yamauchi S, Yamauchi J. J. Phys. Chem. A 2007;111:4612–4619. [PubMed: 17489568]
92. Tenderholt, A.; Hedman, B.; Hodgson, KO. PySpline. Stanford Synchrotron Radiation Laboratory; Stanford, CA: 2006.
93. George, GN. EXAFSPAK. Stanford Synchrotron Radiation Laboratory; Stanford, CA: 2000.
94. Rehr JJ, Albers RC. Rev Mod Phys 2000;72:621–654.
95. Frisch, MJ.; Trucks, GW.; Schlegel, HB.; Scuseria, GE.; Robb, MA.; Cheeseman, JR.; Montgomery, JA., Jr.; Vreven, T.; Kudin, KN.; Burant, JC.; Millam, JM.; Iyengar, SS.; Tomasi, J.; Barone, V.; Mennucci, B.; Cossi, M.; Scalmani, G.; Rega, N.; Petersson, GA.; Nakatsuji, H.; Hada, M.; Ehara, M.; Toyota, K.; Fukuda, R.; Hasegawa, J.; Ishida, M.; Nakajima, T.; Honda, Y.; Kitao, O.; Nakai, H.; Klene, M.; Li, X.; Knox, JE.; Hratchian, HP.; Cross, JB.; Bakken, V.; Adamo, C.; Jaramillo, J.; Gomperts, R.; Stratmann, RE.; Yazyev, O.; Austin, AJ.; Cammi, R.; Pomelli, C.; Ochterski, JW.; Ayala, PY.; Morokuma, K.; Voth, GA.; Salvador, P.; Dannenberg, JJ.; Zakrzewski, VG.; Dapprich, S.; Daniels, AD.; Strain, MC.; Farkas, O.; Malick, DK.; Rabuck, AD.; Raghavachari, K.; Foresman, JB.; Ortiz, JV.; Cui, Q.; Baboul, AG.; Clifford, S.; Cioslowski, J.; Stefanov, BB.; Liu, G.; Liashenko, A.; Piskorz, P.; Komaromi, I.; Martin, RL.; Fox, DJ.; Keith, T.; Al-Laham, MA.; Peng, CY.; Nanayakkara, A.; Challacombe, M.; Gill, PMW.; Johnson, B.; Chen, W.; Wong, MW.; Gonzalez, C.; Pople, JA. Gaussian 03, Revision C.02. Gaussian, Inc.; Wallingford CT: 2004.
96. Tenderholt, Adam L. QMForge, Version 2.1. Stanford University; Stanford, CA, USA:

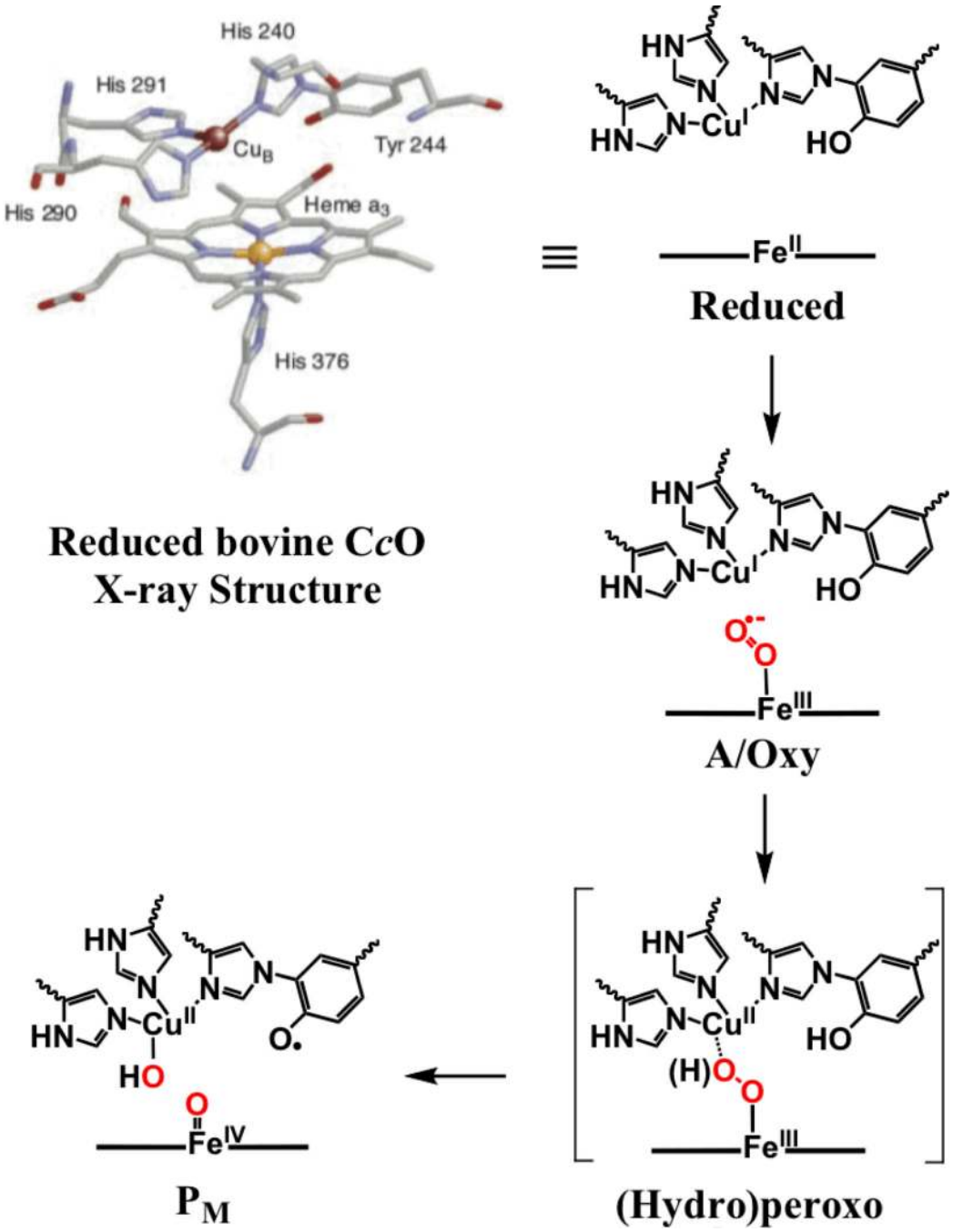

Scheme 1.

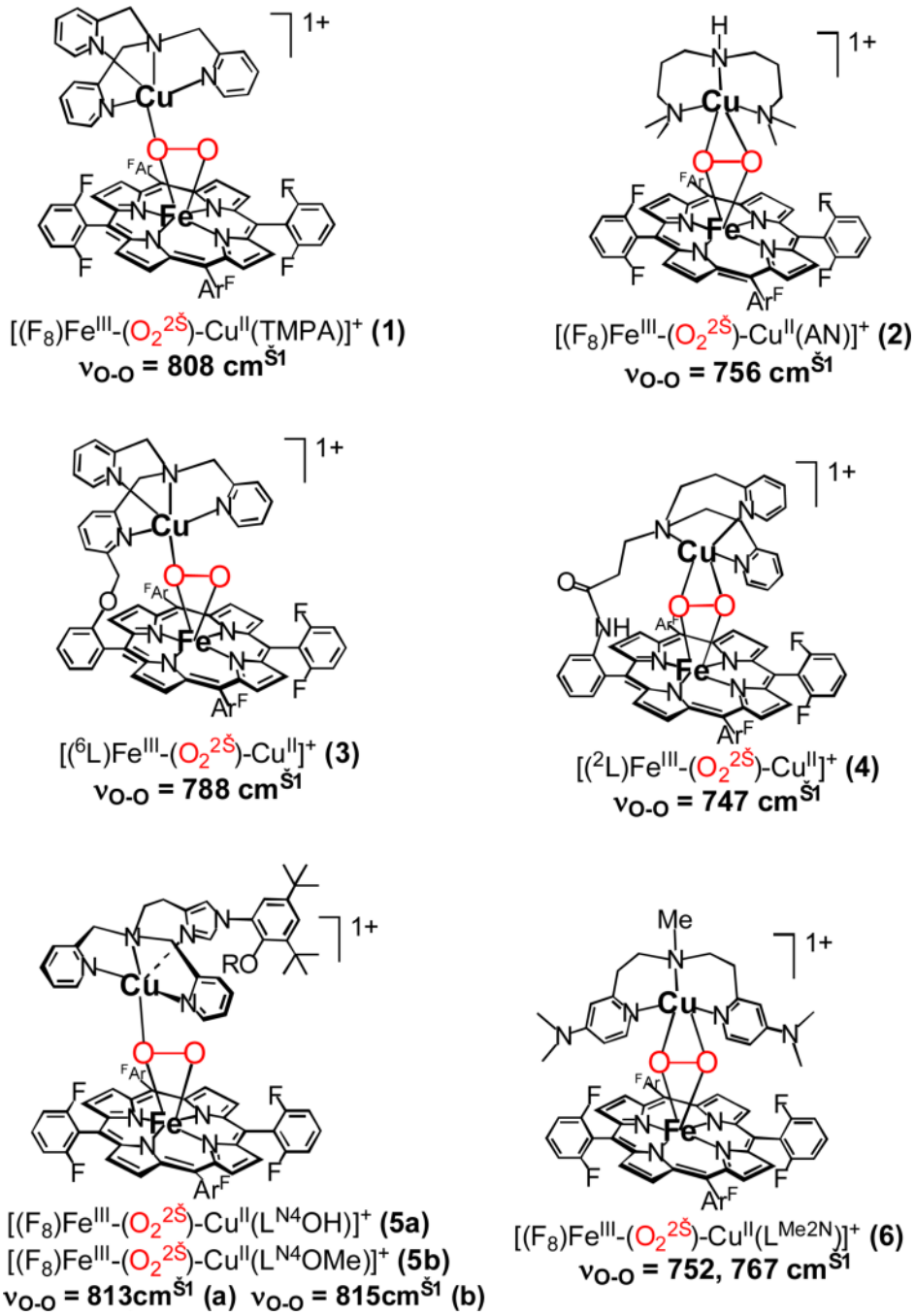

Chart 1.

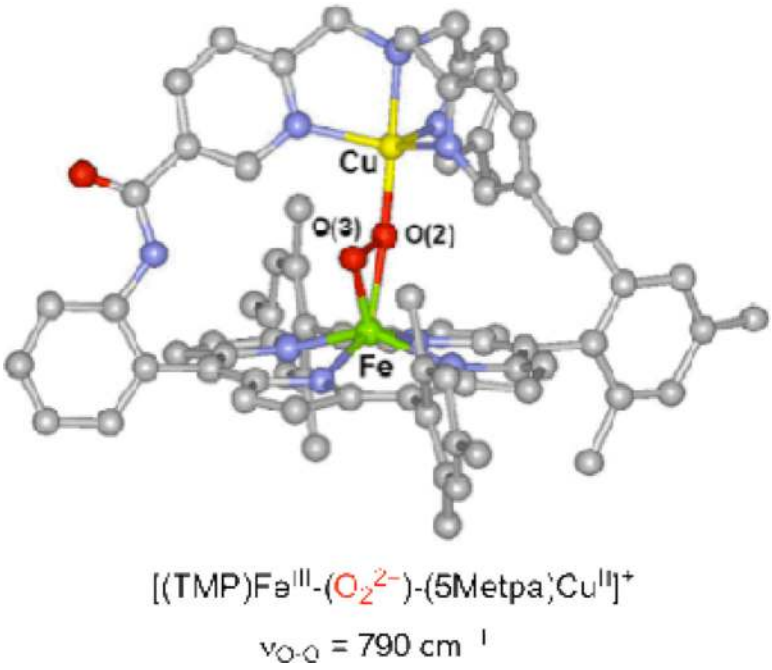

Figure 1.
X-ray structure of [(TMP)Fe^{III}-(O_2^{2-})-(5Metpa)Cu^{II}]$^+$ synthesized and characterized by Naruta and coworkers.

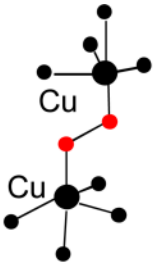

tetradentate Cu chelate
$\nu_{O\check{S}O}$: 805 Š 830 $cm^{\check{S}1}$
Cu...Cu = ~ 4.4 □

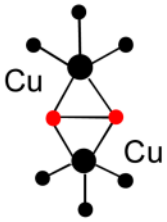

tridentate Cu chelate
$\nu_{O\check{S}O}$: 716 Š 760 $cm^{\check{S}1}$
Cu...Cu = 3.5 Š 3.6 □

Chart 2.

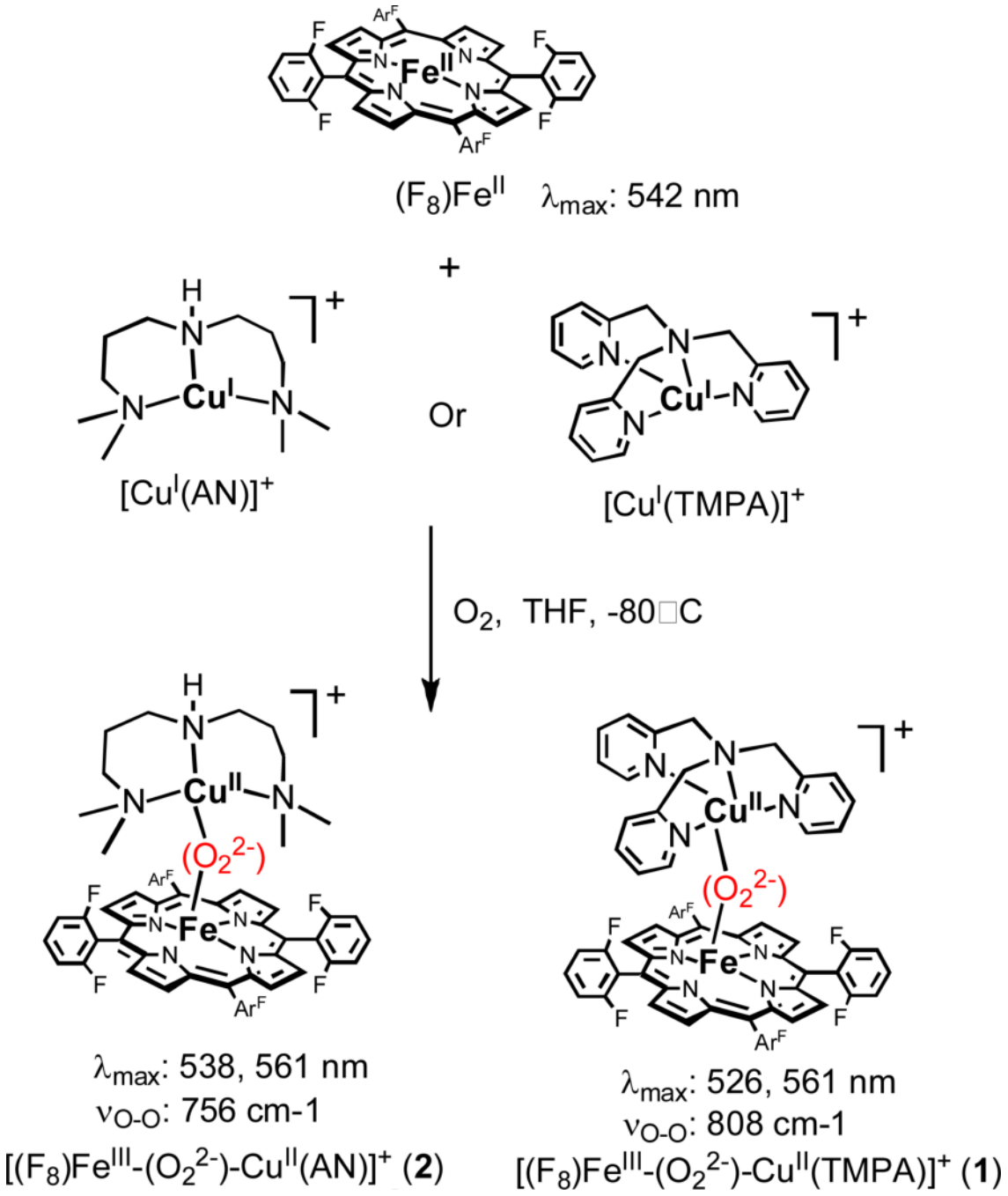

Scheme 2.

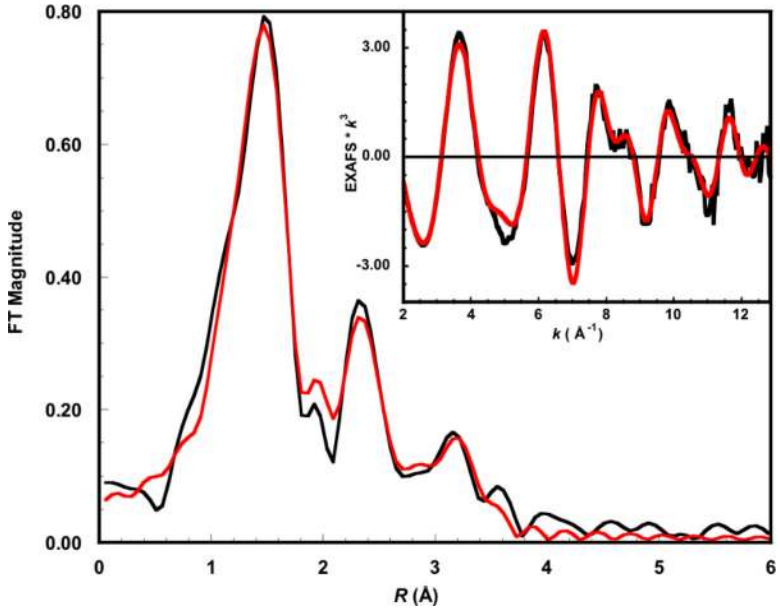

Figure 2.

Cu K-edge EXAFS data to $k = 12.8$ Å^{-1} (inset) and non-phase-shift-corrected Fourier transform of the EXAFS data for **2** in solution. Phase shift in the first shell is ~0.4 Å. Data (▬▬); fit (▬▬).

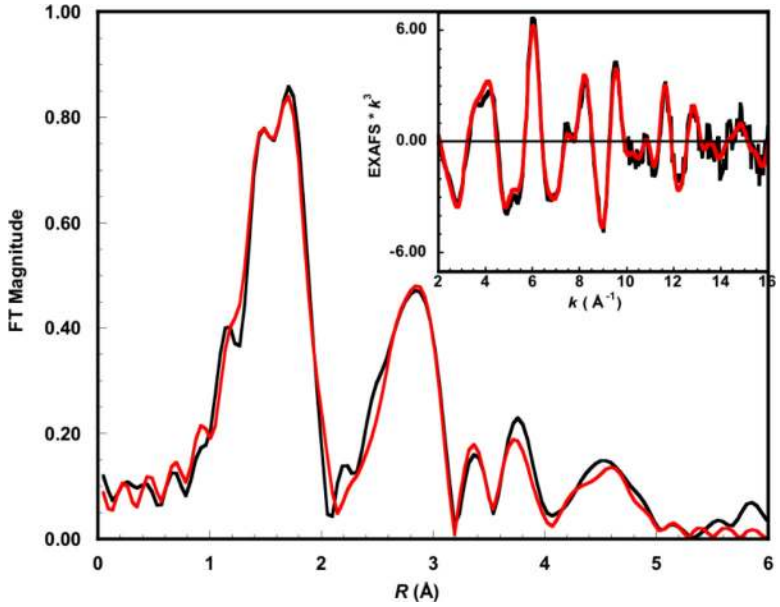

Figure 3.

Fe K-edge EXAFS data to $k = 16$ Å^{-1} (inset) and non-phase-shift-corrected Fourier transform of $[(F_8)Fe^{III}\text{-}O_2\text{-}Cu^{II}(AN)](ClO_4)$ in solution form. Phase shift in the first shell is ~0.4 Å. Data (▬▬); fit (▬▬).

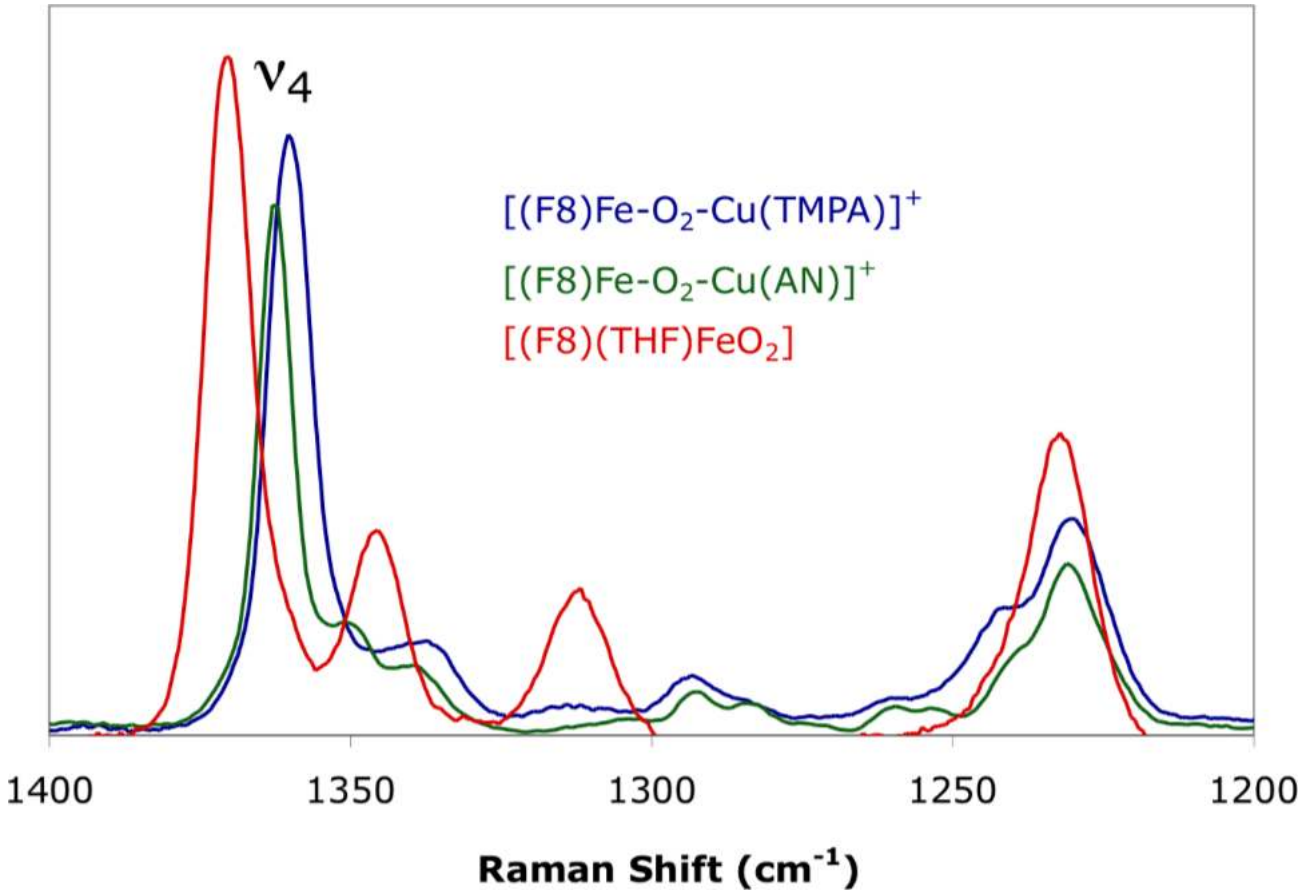

Figure 4.
Resonance Raman spectra with 413 nm excitation of **1** (blue), **2** (green), $[(F_8)(THF)FeO_2]$ (red).

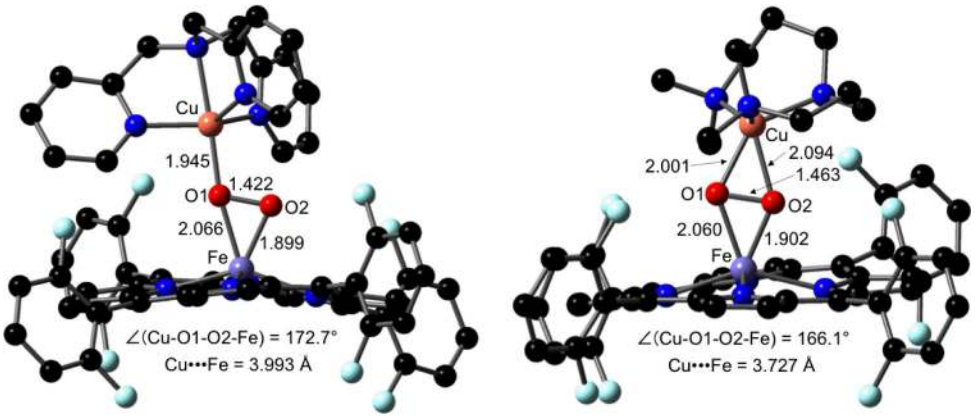

Figure 5.

Unrestricted DFT (BS, $S_T = 2$) optimized molecular structures of $[(F_8)Fe\text{-}(O_2^{2-})\text{-}Cu(TMPA)]^+$ (**1**) (right) and $[(F_8)Fe\text{-}(O_2^{2-})\text{-}Cu(AN)]^+$ (**2**) (left). Hydrogen atoms omitted for clarity.

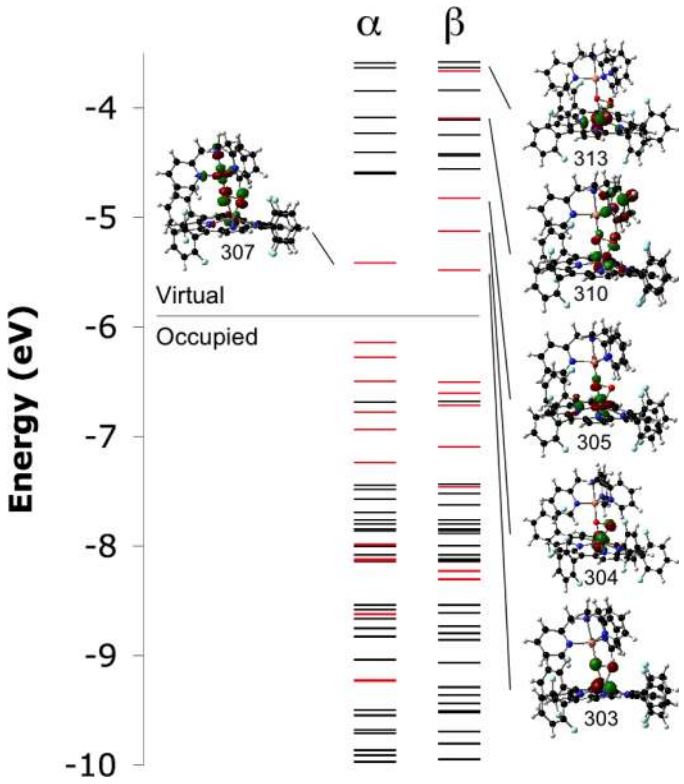

Figure 4.

Isosurface plots (isovalue 0.05 a.u.) of unfilled Cu and Fe d orbitals of **1** from a spin-unrestricted BP86 calculation in the BS ($S_T = 2$) state.

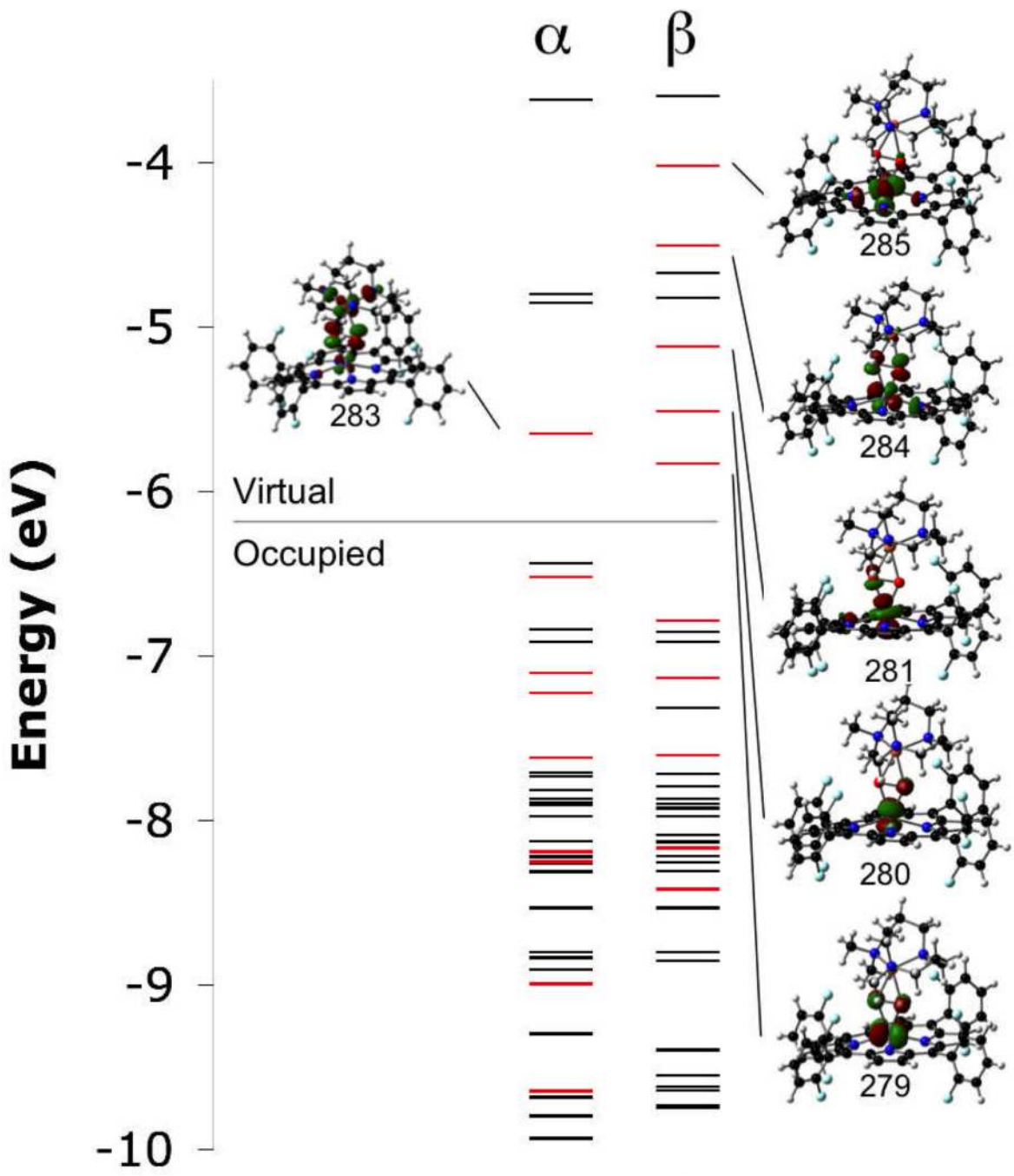

Figure 5.
Isosurface plots (isovalue 0.05 a.u.) of unfilled Cu and Fe d orbitals of **2** from a spin-unrestricted BP86 calculation in the BS ($S_T = 2$) state.

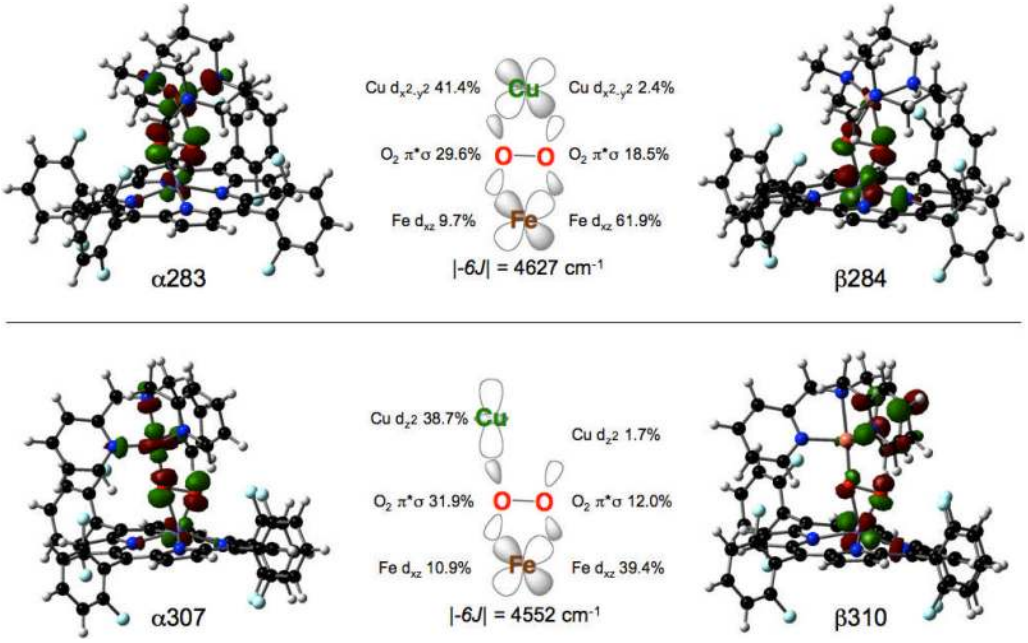

Figure 6.
Isosurface plots (0.05 isovalue) and schematic diagrams of the dominant superexchange pathways of **2** (top) and **1** (bottom).

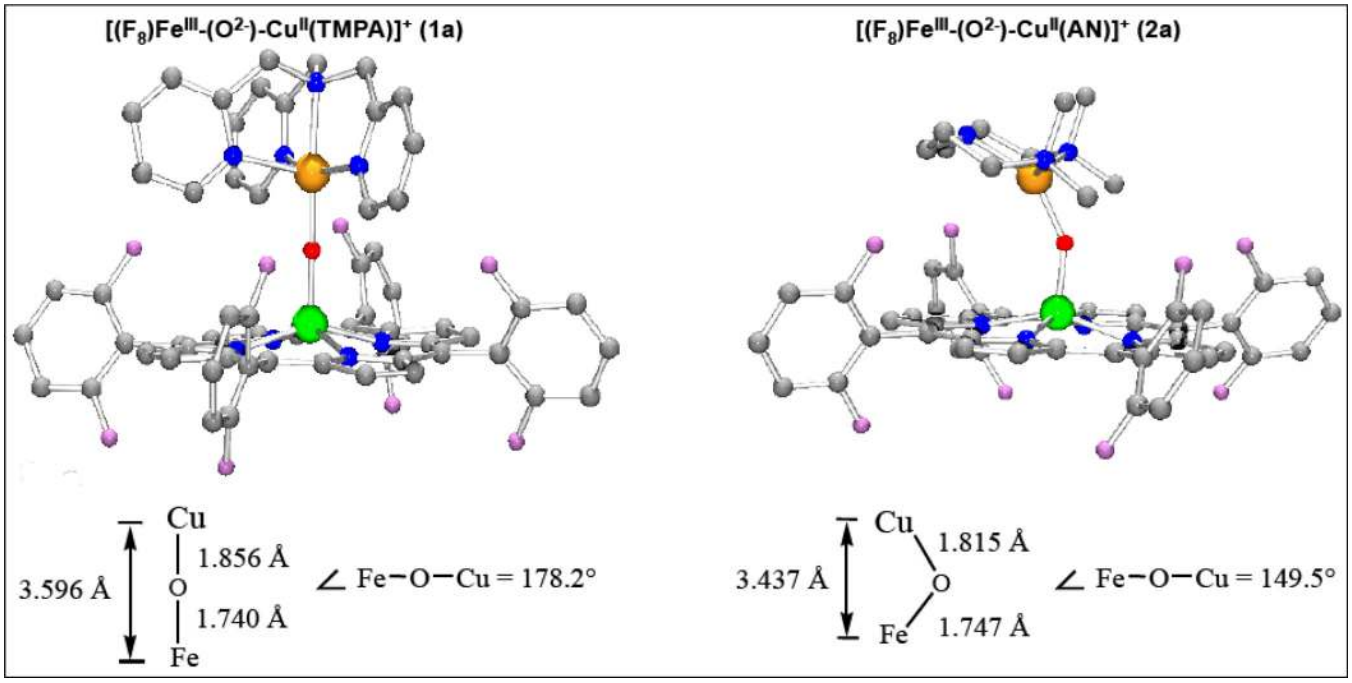

Figure 7.

Core structure depiction of μ-oxo complexes $[(F_8)Fe\text{-}(O^{2-})\text{-}Cu(TMPA)]^+$ (**1a**) and $[(F_8)Fe\text{-}(O^{2-})\text{-}Cu(AN)]^+$ (**2a**). An ORTEP diagram of the cationic portion of **2a** along with other X-ray crystallographic data are given in the Supporting Information.

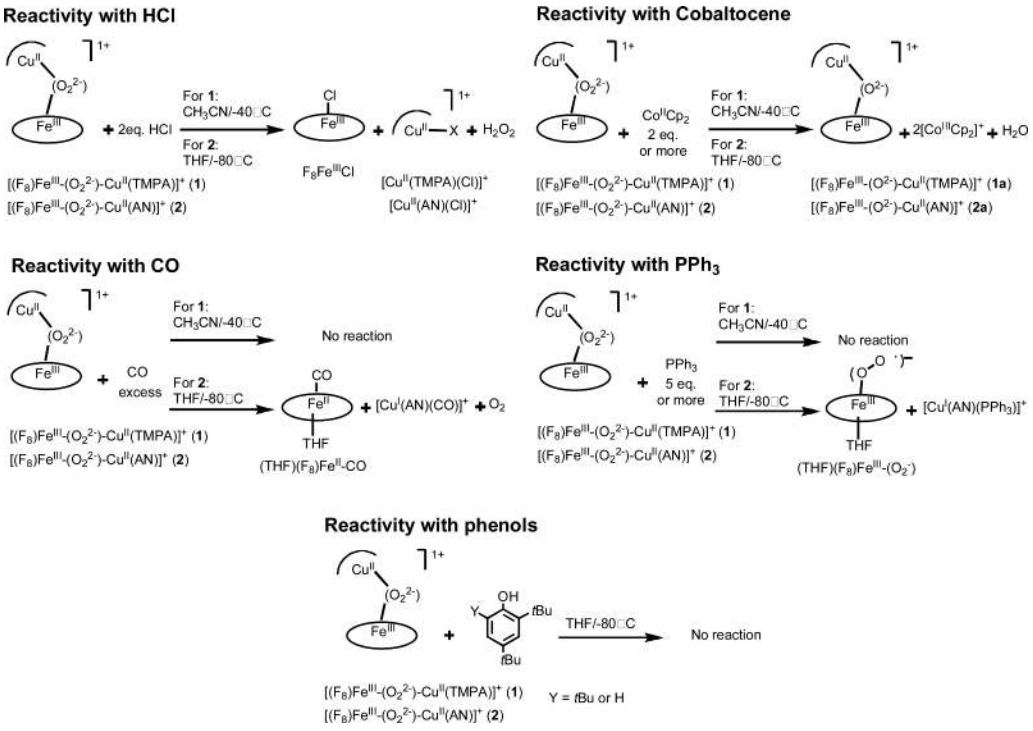

Scheme 3.

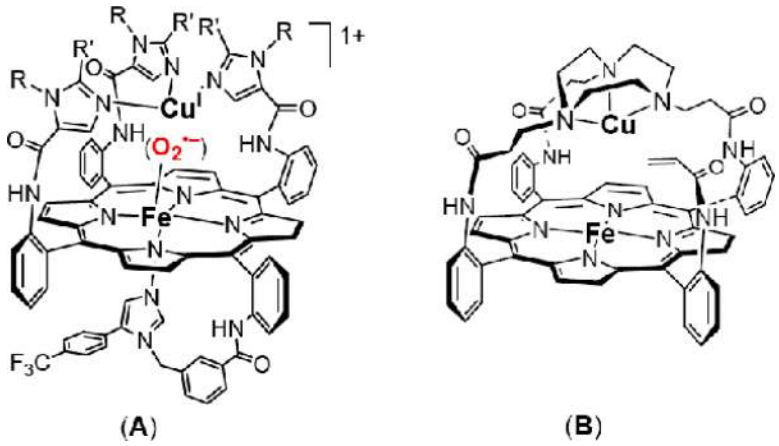

Chart 3.

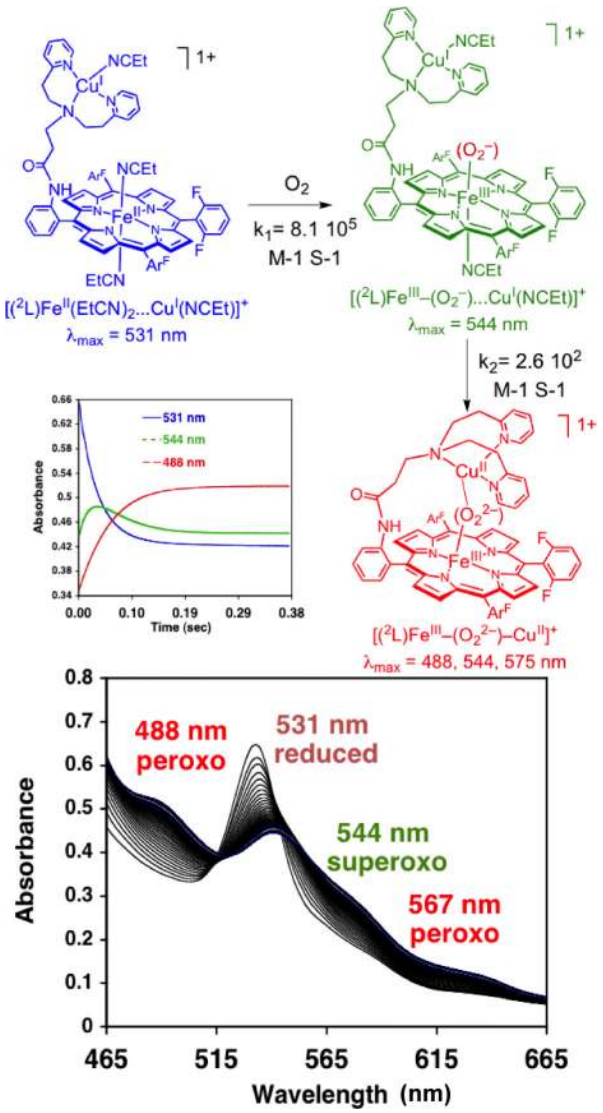

Figure 8.

UV-vis detction of the transient $[(^2L)Fe^{III}\text{-}(O_2^{-})...Cu^{I}(NCEt)]^+$ preceding the formation of $[(^2L)Fe^{III}\text{-}(O_2^{2-})\text{-}Cu^{II}(NCEt)]^+$ by oxygenation of $[(^2L)Fe^{II}\cdots Cu^{I}(NCEt)]^+$ at -90° C in EtCN/ CH_2Cl_2 6%.

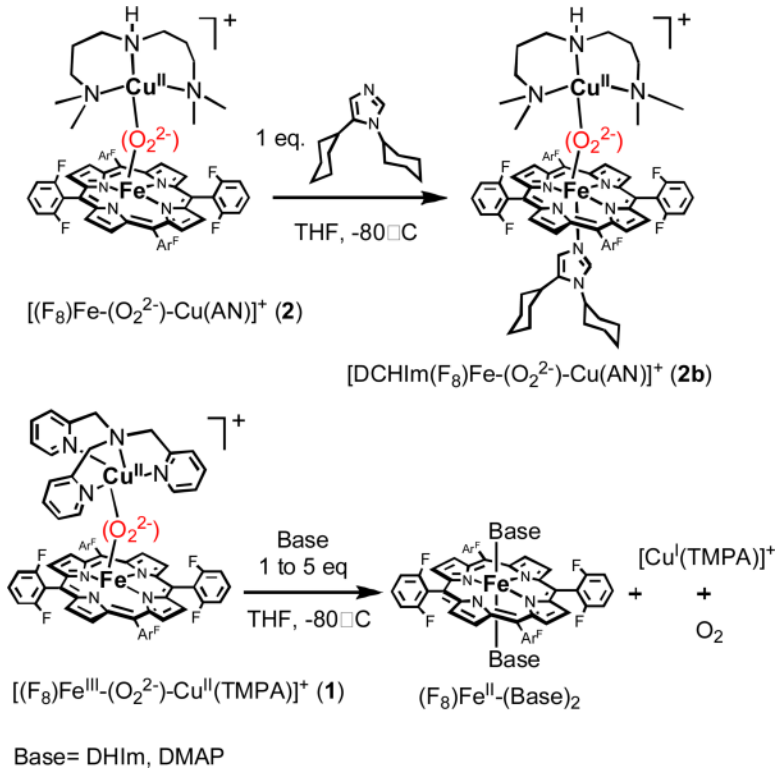

Scheme 4.

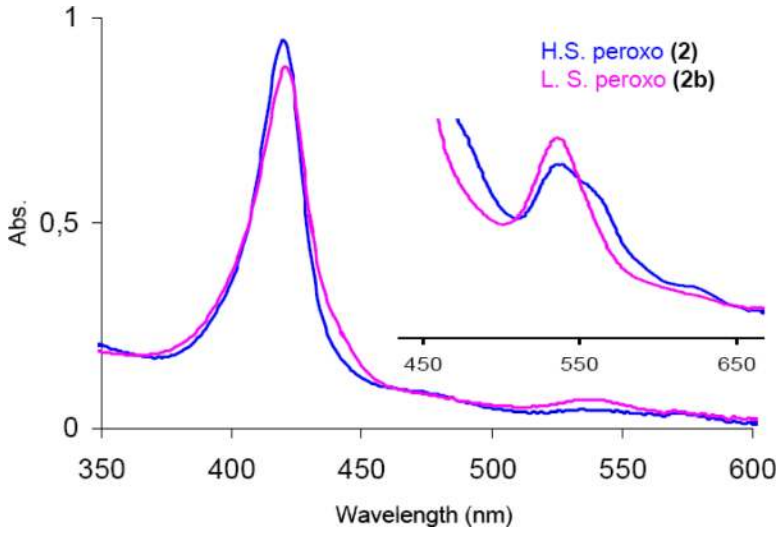

Figure 9.

UV-visible spectra monitoring the generation of the low-spin peroxo complex [DCHIm(F_8)Fe^{III}-(O_2^{2-})-Cu^{II}(AN)]$^+$ (**2b**) (λ_{max}= 421, 537 nm) from the high-spin peroxo complex [(F_8)Fe^{III}-(O_2^{2-})-Cu^{II}(AN)]$^+$ (**2**) (λmax= 418, 538, 561 nm) in THF at -80° C.

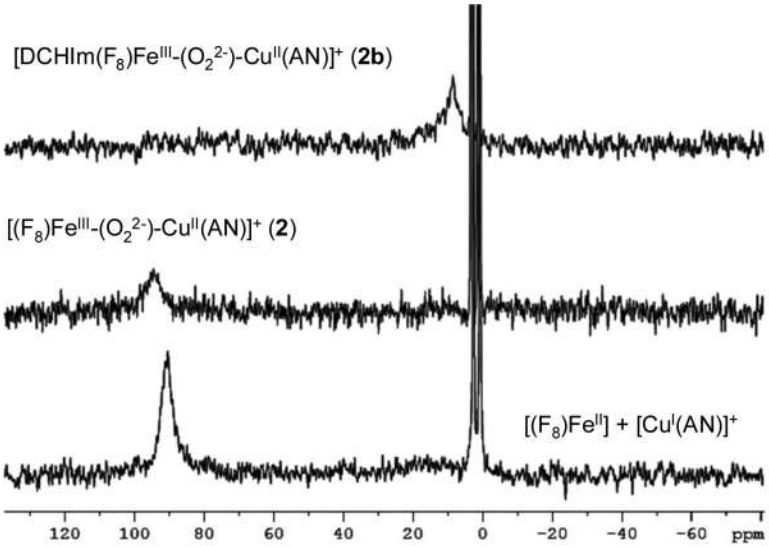

Figure 10.

^{2}H NMR spectra of the generation of $[(F_8)Fe^{III}\text{-}(O_2^{2-})\text{-}Cu^{II}(AN)]^+$ (**2**) and $[DCHIm(F_8)Fe^{III}\text{-}(O_2^{2-})\text{-}Cu^{II}(AN)]^+$ (**2b**) successively from oxygenation of a 1:1 mixture of $[Cu^{I}(AN)]^+$ and the pyrrole-deuterated version of $[(F_8)Fe^{II}]$ (Acetone-d^6 at – 80° C).

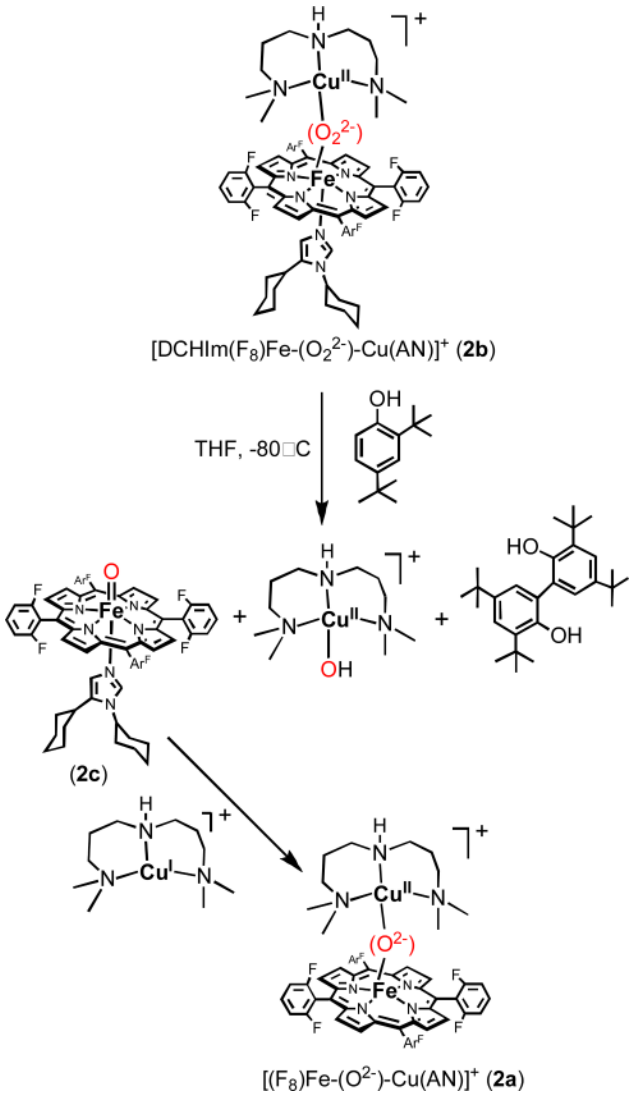

Scheme 5.

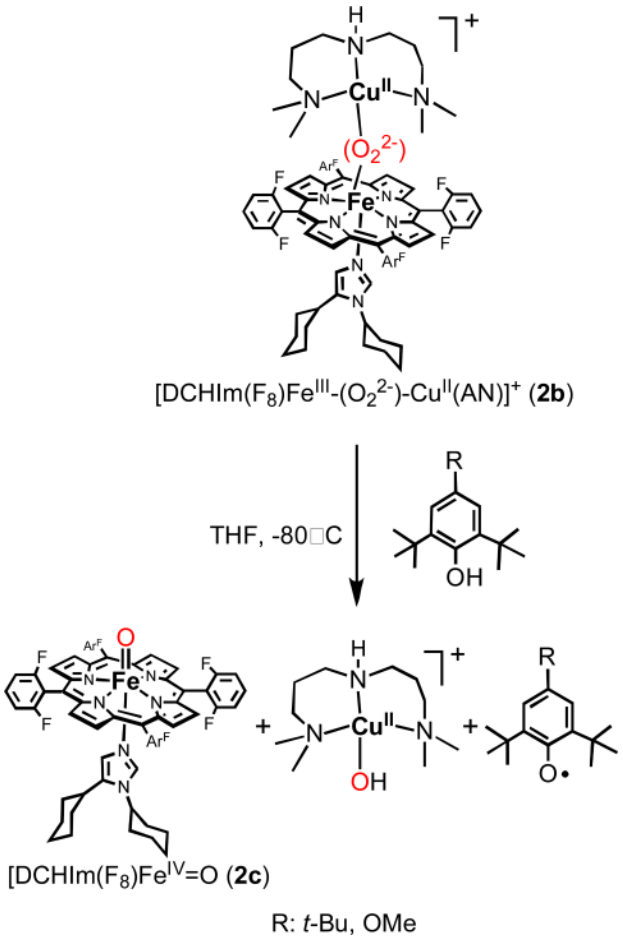

Scheme 6.

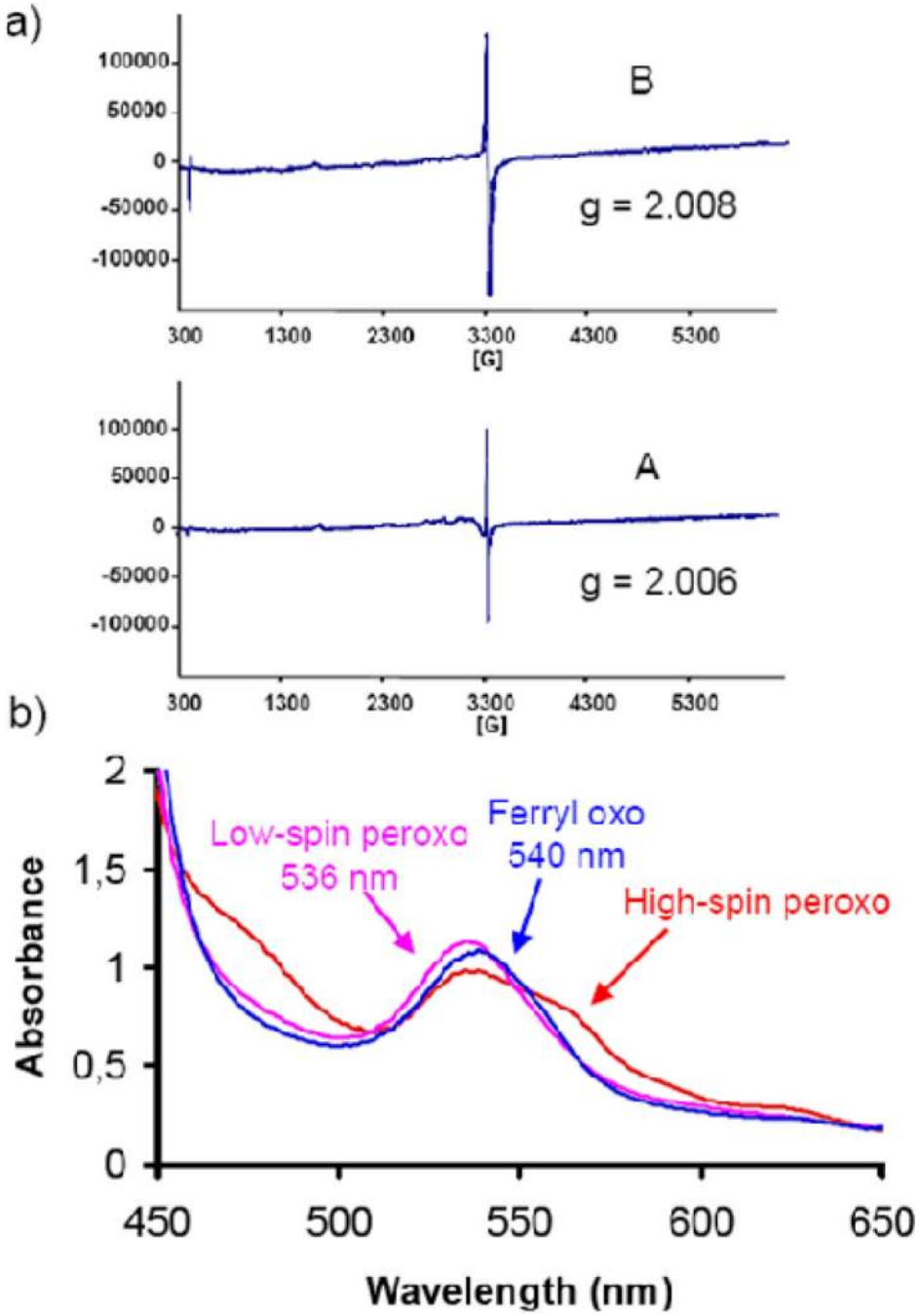

Figure 11.

a) EPR spectra recorded at 77 K of generated phenoxyl radicals by the reaction of [DCHIm(F_8)Fe^{III}-(O_2^{2-})-Cu^{II}(AN)]$^+$ (**2b**) and 2,4,6-tri-*tert*-butylphenol (A) or 2,4-di-*tert*-butyl-4-methoxylphenol (B) at -80° C in THF. As determined in separate experiments, at equal concentrations of a phenoxyl radical with a copper(II) complex, the radical g ~ 2 signal peak intensity is vastly greater than the peak intensities for the g ~ 2.0-to-2.3 signals resultant from the copper(II) ion due to the differences in peak width, which is why the latter is essentially not observable. Also, within the resolution of the EPR experiments conducted, the g-values are indistinguishable.[90,91] b) UV-vis monitoring of the reaction of **2b** with 2,4-di-*tert*-butyl-phenol at -80° C.

Table 1

EXAFS least-squares fitting results for **2**.

Cu Coord./Path	R(Å)[a]	σ^2(Å^2)[b]	ΔE_0(eV)	F[c]	Fe Coord./Path	R(Å)[a]	σ^2(Å^2)[b]	ΔE_0(eV)	F[c]
5 Cu-N/O	2.00	963			1 Fe-O/N	1.94	257		
6 Cu-C	2.92	701			5 Fe-N/O	2.09	397		
16 Cu-N-C	3.22	311	-9.61	0.07	8 Fe-C	3.10	368		
1 Cu-Fe	3.62	653			16 Fe-N-C[d]	3.32	368		
2 Cu-O-Fe	3.75	809			4 Fe-C	3.49	864		
					1 Fe-Cu	3.64	370	-2.09	0.23
					2 Fe-O-Cu[d]	3.71	370		
					5 Fe-C	3.81	461		
					12 Fe-N-C	4.38	513		
					16 Fe-C-C	4.91	377		
					8 Fe-C-C	4.98	291		

[a] The estimated standard deviations in R for each fit is ±0.02 Å.

[b] The σ^2 values are multiplied by 10^5.

[c] The error, F, is given by $\Sigma[(\chi_{obsd} - \chi_{calcd})^2 k^6]/\Sigma[(\chi_{obsd})^2 k^6]$.

[d] The σ^2 for the multiple scattering path is linked to that of the corresponding single scattering path. The errors in ΔE_0 values are ±0.22 eV for Cu and ±0.27 eV for Fe. The estimated errors in σ^2 are 5-30%. The error in coordination number is 20-25% and that in the identity of the scatterer Z is ±1.

Table 2

Selected DFT optimized bond distances (Å) and angles (°) of models $[(F_8)Fe\text{-}(O_2^{2-})\text{-}Cu(TMPA)]^+$ (**1**) and $[(F_8)Fe\text{-}(O_2^{2-})\text{-}Cu(AN)]^+$ (**2**).

	DFT optimized coordinates of 1	DFT optimized coordinates of 2
Cu—O (Å)	1.945, 2.764	2.094, 2.001
O—O (Å)	1.433	1.463
Fe—O (Å)	2.066, 1.889	2.060, 1.902
Fe···Cu (Å)	3.994	3.727
Cu—O—O (°)	109.4	72.5, 65.7
Fe—O—O (°)	75.7, 62.4	74.2, 62.7
Fe—O—O—Cu (°)	172.7	166.1

Table 3

Mulliken population analysis of molecular orbitals from a spin-unrestricted BP86 calculation of **1** in the BS ($S_T = 2$) state.

orbital	level	occ	E(eV)	Cu	O_2	Fe	rest
α307	Cu – $O_2\pi^*_\sigma$	0	-5.417	38.7	31.9	10.9	18.5
β313	Fe $_{x^2-y^2}$	0	-3.661	0.1	2.46	67.5	30.0
β310	Fe xz	0	-4.108	1.7	12.0	39.4	47.0
β305	Fe $_{z^2}$	0	-4.825	2.3	6.2	70.4	21.1
β304	Fe yz	0	-5.126	0.0	9.2	66.2	24.7
β303	Fe xy - $O_2\pi^*_v$	0	-5.482	1.2	15.9	76.7	6.2
		spin density		-0.36	0.20, 0.02	3.76	

Table 4

Mulliken population analysis of molecular orbitals from a spin-unrestricted BP86 calculation of **2** in the BS ($S = 2$) state.

orbital	level	occ	E(eV)	Cu	O_2	Fe	rest
α283	Cu – $O_2\pi^*_\sigma$	0	-5.653	41.4	29.6	9.7	19.3
β285	Fe x^2-y^2	0	-4.021	0.3	2.5	68.3	28.9
b284	Fe xz	0	-4.508	2.4	18.5	61.9	17.2
β281	Fe z^2	0	-5.121	1.2	5.9	75.6	17.3
β280	Fe yz	0	-5.511	0.6	5.6	72.6	21.2
β279	Fe xy - $O_2\pi^*_v$	0	-5.834	0.5	13.4	80.5	5.7
		spin density		-0.56	0.10, -0.19	0.85	